

Lower Crustal Heterogeneity and Fractional Crystallisation Control Evolution of Small Volume Magma Batches at Ocean Island Volcanoes (Ascension Island, South Atlantic)

K. J. CHAMBERLAIN^{1,2*}, J. BARCLAY³, K. J. PREECE⁴, R. J. BROWN¹ and J. P. DAVIDSON^{1§}

¹ DEPARTMENT OF EARTH SCIENCES, DURHAM UNIVERSITY, DURHAM, DH1 3LE, UK

² SCHOOL OF ENVIRONMENTAL SCIENCES, UNIVERSITY OF DERBY, DERBY, DE22 1GB, UK

³ SCHOOL OF ENVIRONMENTAL SCIENCES, UNIVERSITY OF EAST ANGLIA, NORWICH, NR4 7TJ, UK

⁴ DEPARTMENT OF GEOGRAPHY, COLLEGE OF SCIENCE, SWANSEA UNIVERSITY, SINGLETON PARK, SWANSEA, SA2 8PP, UK

§ Deceased

*Corresponding author. Phone (+44-1332-592971)

Email address: k.chamberlain@derby.ac.uk

ABSTRACT

Ocean island volcanoes erupt a wide range of magmatic compositions via a diverse range of eruptive styles. Understanding where and how these melts evolve is thus an essential component in the anticipation of future volcanic activity. Here we examine the role of crustal structure and magmatic flux in controlling the location, evolution and ultimately composition of melts at Ascension Island. Ascension Island, in the South Atlantic, is an ocean island volcano which has produced a continuum of eruptive compositions from basalt to rhyolite in its 1Myr subaerial eruptive history. Volcanic rocks broadly follow a silica-undersaturated subalkaline evolutionary trend, and new data presented here show a continuous compositional trend from basalt through trachyte to rhyolite. Detailed petrographic observations are combined with *in situ* geochemical analyses of crystals and glass, and new whole-rock major and trace element data from mafic and felsic pyroclastic and effusive deposits that span the entire range in eruptive ages and compositions found on Ascension Island. These data show that extensive fractional crystallisation is the main driver for the production of felsic melts for Ascension Island; a volcano built on thin, young, oceanic crust. Strong spatial variations in the compositions of erupted magmas reveal the role of a heterogeneous lower crust; differing degrees of interaction with a zone of plutonic rocks are responsible for the range in mafic lava compositions, and for the formation of the central and eastern felsic complexes. A central core of nested, small-scale plutonic, or mush-like, bodies inhibits the ascent of mafic magmas, allowing sequential fractional crystallisation within the lower crust, and generating felsic magmas in the core of the island. There is no evidence for magma mixing preserved in any of the studied eruptions, suggesting that magma storage regions are transient, and material is not recycled between eruptions.

Keywords: Ascension Island, ocean island volcanism, fractional crystallisation, magmatic processes, oceanic crust

INTRODUCTION

Ocean island volcanoes remain enigmatic in terms of their origin (Niu *et al.*, 2011), evolution and ability to produce a range of magmatic compositions and eruptive activity. Many ocean islands such as Iceland, Socorro, and the archipelagos of Hawaii, the Galapagos and the Canaries have been studied in detail (e.g. Sparks & Sigurdsson, 1987; Geist *et al.*, 1988; Ablay *et al.*, 1998; Geist *et al.*, 1995; Bohrsen *et al.*, 1996; Harpp & White, 2001; Koppers & Staudigel, 2005; Carracedo *et al.*, 2007; Carley *et al.*, 2011; Mancini *et al.*, 2015), but some ocean island volcanoes remain relatively poorly understood (e.g. the Azores, St Helena), and yet still pose a significant hazard to populations often living proximal to volcanic vents. Ascension Island, in the South Atlantic, is an example of the latter. It is small (subaerial dimensions of 8 km by 12 km), has no associated hotspot trace (cf. Hawaii, the Canaries; e.g., Zhao, 2004; Montelli *et al.*, 2004) and has erupted magmas with a wide range of compositions (Daly, 1925; Coombs, 1963; Weaver *et al.*, 1996; Kar *et al.*, 1998; Jicha *et al.*, 2013). This compositional diversity is matched by a diversity in eruption styles and range of volcanic deposits (Weaver *et al.*, 1996; Kar *et al.*, 1998; Hobson, 2001; Preece *et al.*, 2016).

Evolved, more felsic, melts have the potential to generate significant hazards at ocean island volcanoes, and thus understanding where and how they evolve in the crust is imperative to forecasting future styles of eruption. The various means by which felsic magmas evolve have the potential to produce a range of compositions, which affects magma viscosity (Papale *et al.*, 1998) and the amount of dissolved volatiles, all of which contribute to the mode of evacuation of magma from crustal storage regions (e.g. Eichelberger, 1995; Giordano *et al.*, 2004). At ocean islands these silicic melts are considered to be generated via: anatexis of crustal material by hotter mafic melts (e.g. Sverrisdottir, 2007; Carley *et al.*, 2011; Kuritani *et al.*, 2011); extensive crystal fractionation from a more primitive mafic magma (e.g., Geist *et al.*, 1995; Mungall & Martin, 1995; Larrea *et al.*, 2014; Jeffrey *et al.*,

2016); by direct derivation from mantle partial melting (Ashwal *et al.*, 2016) or through a combination of these processes (e.g. Bohrsen & Reid, 1997; Wiesmaier *et al.*, 2013; Sliwinski *et al.*, 2015). Understanding the relative importance of these processes in any one setting has significant implications for understanding the relationships between the timescales of magma genesis, magmatic heat flux and potential triggering mechanisms of eruptions.

Ascension Island has produced more than 70 explosive eruptions of felsic magma in its ~ 1 Myr subaerial history (Preece *et al.*, 2016), in addition to numerous eruptions that produced scoria cones, mafic lava flows, and felsic lava flows and domes. The erupted rocks have largely been used to investigate the origins of Ascension Island magmatism (e.g. Harris *et al.*, 1982; Weaver *et al.*, 1987, 1996; Weis *et al.*, 1987; Kar, 1997; Kar *et al.*, 1998; Paulick *et al.*, 2010). As yet, little is understood about the magmatic plumbing system on Ascension Island and the control it exerts on magmatic composition and styles of eruptive activity. Thus, we focus here on the relationship between the mafic and felsic magmatism on Ascension, utilising whole-rock major and trace element data, and a comprehensive suite of *in situ* crystal major and trace element data by EPMA (electron probe microanalysis) and LA-ICP-MS (laser ablation inductively coupled plasma mass spectrometry). Samples studied here represent the products of 22 eruptions representing the full range in composition and eruptive styles presented by subaerial volcanism on Ascension Island. By combining these data with previous isotopic work and work on a compositionally-zoned fall deposit (Chamberlain *et al.*, 2016), we present a model for the magmatic plumbing system of Ascension Island in which felsic magmas evolve and stall in the lower crust, and highlight the role of crustal structure in the evolution of felsic melts on ocean islands with a low magmatic flux. Other potentially low magmatic flux ocean islands include the archipelagos of the Azores and Cape Verde islands, and thus the results of this study could be tested at other ocean islands around the world.

ASCENSION ISLAND

Ascension Island (7° 56' S; 14° 22' W) is located in the southern Atlantic Ocean, 90 km west of the Mid-Atlantic Ridge (MAR) and 50 km south of the Ascension Fracture Zone (AFZ; Fig. 1). Volcanism began on the sea floor 5 – 6 Myr ago, and subaerial volcanism has occurred from ~1 Ma to present (Kar *et al.*, 1998; Minshull *et al.*, 2010; Paulick *et al.*, 2010; Jicha *et al.*, 2013; Preece *et al.*, 2016). The most recent eruption at Ascension Island has been dated by ^{40}Ar - ^{39}Ar dating to 0.51 ± 0.18 ka (Preece *et al.*, 2018) - with no evidence for pauses in eruptive activity of greater than 130 kyr throughout the 1 million years of subaerial volcanism (Jicha *et al.*, 2013).

Crustal structure of Ascension Island

Ascension Island is built on 5 – 7 Myr old oceanic crust (Klingelhöfer *et al.*, 2001; Paulick *et al.*, 2010) on, or close to, the MAR. Due to the OIB-like trace element affinities of Ascension mafic lavas (Harris, 1983; Weaver *et al.*, 1996), it has been suggested that magmatism at Ascension Island is the product of a shallow mantle plume, rising at the MAR then diverted along the Ascension Fracture Zone (AFZ, Fig. 1; Burke & Wilson, 1976; Montelli *et al.*, 2006). However, seismic surveys have revealed a crustal structure that cannot be reconciled with a classic intra-plate ocean island (i.e. a lack of lithospheric flexure, cf. Klingelhöfer *et al.*, 2001), and instead suggest that significant growth of the Ascension Island edifice occurred on the MAR-axis. The seismic surveys show that the crust is 12 – 13 km thick under Ascension, with over-thickening of layer 3, to 7 km thick (Klingelhöfer *et al.*, 2001). Active-source seismic tomographic studies failed to find evidence for magmatic underplating beneath the island, suggesting that the island's origins are not related to a hot spot (Evangelidis *et al.*, 2004). Additionally, Evangelidis *et al.* (2004) located areas of

anomalously high velocity within the middle crust, which were inferred to be the crystallised remains of a relict magma chamber.

Geochemical insights into the source of Ascension Island

OIB-like trace element patterns have been recorded from magmas erupted on Ascension Island, and spurred extensive research into the origins of the magmatism, in particular its relationship to an undefined mantle anomaly and the proximal MAR. Sr and Nd isotopic data show little difference between the subaerial and the (volumetrically dominant) submarine products of Ascension: $^{143}\text{Nd}/^{144}\text{Nd}$ varies between 0.51292 and 0.51310, and significant variation in $^{87}\text{Sr}/^{86}\text{Sr}$ has been measured - between 0.70276 and 0.70656 (Fig. 2a; Weaver *et al.*, 1996; Kar *et al.*, 1998; Paulick *et al.*, 2010). Submarine products have distinctly different Hf isotopic characteristics to the subaerial products studied here, and this has lead previous workers to suggest that the mantle source tapped by the submarine stage is no longer present (Fig. 2c; Paulick *et al.*, 2010). There is little variation in Sr, Nd or Pb isotopic characteristics with time in the subaerial edifice (Kar, 1997; Paulick *et al.*, 2010; Jicha *et al.*, 2013), nor is the significant variation in $^{87}\text{Sr}/^{86}\text{Sr}$ coupled to variations in $^{143}\text{Nd}/^{144}\text{Nd}$ (Fig. 2a). The large variation in $^{87}\text{Sr}/^{86}\text{Sr}$ has been suggested to reflect post-emplacement alteration of samples (especially evolved rocks) by seawater-derived groundwater fluids as the samples were not acid-leached prior to analysis (Kar *et al.*, 1998; cf., Davidson *et al.*, 1997). Due to the low Sr-contents of the Ascension magmas, they are particularly susceptible to alteration either through post-emplacement alteration, or by small degrees of assimilation of seawater-altered lithologies (Kar *et al.*, 1998).

Previous studies utilised the trace element variation in basaltic magmas erupted on Ascension Island to infer their source composition and to define three main magmatic groups, principally based on Zr/Nb ratios (Weaver *et al.*, 1996; Kar, 1997). The oldest and most

voluminous magma type in submarine and subaerial Ascension is represented by the high Zr/Nb ($\text{Zr/Nb} > 5.7$) mafic lavas (principally exposed on the south coast, Fig. 1; Weaver *et al.*, 1996; Kar, 1997). Low Zr/Nb ($\text{Zr/Nb} < 4.3$) lavas are relatively spatially restricted, outcropping only in the southwest (Fig. 1). Intermediate Zr/Nb lavas ($\text{Zr/Nb} 4.3 - 5.7$) are the most common lavas in the subaerial history (but have erupted coevally with high and low Zr/Nb lavas), and dominate the northern and western regions (Fig. 1; Weaver *et al.*, 1996; Kar, 1997; Jicha *et al.*, 2013). The origins of these mafic lavas, and the process responsible for their variation has been related to varying degrees of partial melting of a consistent source, or melting of different mantle regions with differing mineralogy (Weaver *et al.*, 1996; Kar, 1997; Jicha *et al.*, 2013). Isotopic and trace element data for the mafic lavas types (Weaver *et al.*, 1996; Kar *et al.*, 1998; Paulick *et al.*, 2010; Jicha *et al.*, 2013), show that fractional crystallisation alone cannot reproduce the variability in Ti, Ta and Nb (Fig. 2c), and that variations in degree of partial melting, or source composition are more likely causes of this variability (Jicha *et al.*, 2013). As the Zr/Nb ratios are more characteristic of variations during the initial production of magma (source lithology or degree of partial melting), they will not be used here to investigate the nature of the magmatic plumbing system.

Evolution and distribution of volcanism at Ascension Island

The magmatism on Ascension Island defines a transitional to mildly-alkaline, silica under-saturated array from olivine basalt - hawaiiite - mugearite - benmoreite - trachyte - rhyolite (Daly, 1925; Weaver *et al.*, 1996; Fig. 3). Mafic volcanic products are erupted all across the island (Fig. 1), while felsic products are limited to central and eastern areas (Fig. 1). Previous authors have divided the silicic eruptive products into two main centres: an older (Kar *et al.*, 1998; Hobson, 2001; Jicha *et al.*, 2013) central felsic region, which contains the oldest dated

exposed lava on the island (at 1094 ka, Jicha *et al.*, 2013), and a younger eastern complex (youngest published Ar-Ar date of 52 ± 3 ka; Jicha *et al.*, 2013; Fig. 1). Felsic magmas are inferred to be the product of high degrees of fractional crystallisation (Fig. 2c; Weis *et al.*, 1987; Kar *et al.*, 1998; Webster & Rebbert, 2001; Jicha *et al.*, 2013), originating chiefly from similar mafic melts to those erupted around the peripheries of the felsic complexes (both high and intermediate Zr/Nb basalts have been suggested as parental melts; Figs 1, 2c; Weaver *et al.*, 1996; Kar *et al.*, 1998; Jicha *et al.*, 2013).

The nature of the magmatic plumbing system on Ascension Island has not been established, yet fractional crystallisation is suggested as the dominant process for the formation of felsic melts (Kar *et al.*, 1998; Jicha *et al.*, 2013). There is only limited geochemical evidence for interaction between evolved magma batches to date (Kar *et al.*, 1998; Chamberlain *et al.*, 2016). Melt inclusion compositions and whole-rock isotopic ratios of plutonic lithic clasts have been used to infer a genetic association between the plutonic lithics and the spectrum of volcanic rocks (Roedder & Coombs, 1967; Harris *et al.*, 1982; Weis *et al.*, 1987; Webster & Rebbert, 2001). These studies have suggested that the formation of the granitic plutonic bodies occurred at temperatures of 710 – 865 °C, and pressures of 200 – 300 MPa (Webster & Rebbert, 2001, and references therein). Recent work on the crystal cargo and melt inclusions from a compositionally-zoned fall deposit on the island (Chamberlain *et al.*, 2016) supports the hypothesis that felsic magmas evolved through closed-system evolution on Ascension (as suggested by Harris, 1986 and Weaver *et al.*, 1987), with no petrological or textural evidence for magma mixing or multiple phases of stalling. We test the relevance of this model for the generation of all felsic magmas on Ascension Island, and use these data to improve our understanding of the temporal and spatial relationships between felsic and mafic volcanism.

SAMPLING & METHODOLOGY

The volcanic rocks on Ascension Island are extremely diverse and provide evidence for Hawaiian, Strombolian and as well as more explosive (Subplinian to Plinian) eruptions, as well as phreatomagmatic activity. These products include lava flows and domes, pumice, scoria and ash fall deposits and pyroclastic density current deposits (Preece *et al.*, 2016). The products of 22 representative eruptions that cover the full range in magmatic composition, eruptive style (Fig. 3) and the temporal and spatial extent of subaerial volcanism were analysed in detail to capture this range (Fig. 1; Table 1). Mafic lavas outcrop widely across the island and dominate its submarine history (see Nielson & Sibbett, 1996; Minshull *et al.*, 2010). Mafic lava samples were selected to represent the main fields of mafic lava flows found on Ascension Island: the north coast (Sisters; samples AI14-411, AI14-471); the south-west region (Wideawakes; samples AI14-445, AI14-449); the south-east (Letterbox, AI14-423, AI14-429); the south coast (South Coast, AI14-514, AI14-522). In this way, the spatial and temporal variability (old *versus* young lavas from the same eruptive centres) of mafic lavas on Ascension Island can be examined (Fig. 1; Table 1). Felsic samples come from effusive and explosive products, including samples from the older central felsic complex (AI-94, AI-103, AI15-621, AI14-459, AI14-488, AI14-493) and the younger eastern felsic complex (AI14-511, AI14-419, AI14-618, AI14-428, AI14-435, AI14-438). These samples were chosen to ensure a wide spatial and temporal sampling of the felsic volcanism (for individual sample names see Table 1).

Scoria and pumice samples were sieved to > 16 mm (or 8 mm if juvenile clasts were less than 16 mm) and all lithic clasts were removed by hand. These samples were then thoroughly cleaned by removing any adhering matrix or oxidised rind followed by soaking in (frequently changed) milli-RO water for a minimum of one week. Lava was treated by removing external, altered material then washed to remove any cutting fluid. All samples

were then dried thoroughly at 60 °C prior to crushing. An aliquot of each sample was selected to mill for X-ray fluorescence (XRF) analysis at the University of East Anglia (UEA) using a Bruker-AXS S4 Pioneer. For major elements (>0.5 wt %) analyses of multiple international standards yielded uncertainties $\leq \pm 0.5$ wt % (2σ), except for SiO₂ which yielded an uncertainty of ± 1.06 wt % (2σ). Values of the standards compared with published values yielded accuracies within 2% for all major elements, except for MnO, CaO and P₂O₅ where values were within 9% of published values; for full details of standards used, and their precision see Supplementary Data Electronic Appendix 1. Trace element analyses of selected standards gave uncertainties < 5% (2σ) for V, Cr, Ni, Cu, Zn, Rb, Sr, Y, Zr, Nb, Mo and Ba, with uncertainties <10% for As, Ce and U. For full details see Electronic Appendix 1.

The remaining material was prepared for *in situ* analysis of major and trace elements in crystals and glass. Thin sections were made of lava samples, whilst pyroclastic samples were crushed, sieved into various size fractions (< 2 mm), before crystal and glass separates (from the 0.5 – 1 mm size fraction) were hand-picked and mounted into low-activity epoxy discs, and polished.

Prior to *in situ* analyses, back-scattered electron (BSE) images were taken of all thin sections and epoxy blocks to identify crystal phases present, any zonation preserved in crystals and to locate suitable analytical spots. These images were obtained on a JEOL JSM 5900LV scanning electron microscope (SEM) at UEA. Percentages of phases were calculated using ImageJ® software of transmitted light photomicrographs and BSE imagery, by filtering images based on colour or greyscale characteristics.

In situ major element analyses were obtained by EPMA using a JEOL JXA 8230 system at Victoria University of Wellington (VUW), or using a CAMECA SX100 at Edinburgh University, both using wavelength-dispersive spectrometry. Operating conditions varied depending on the phases and elements analysed, but the precision of standard analyses

of major elements (>1 wt % concentration) were always within 2 relative % (2 s.d.); with slightly higher uncertainties for minor elements (see Supplementary Data Electronic Appendix 1 for further details on accuracy and precision of secondary standards). Due to their hydrous nature, only glass analyses with totals of <93 wt % were set aside; values for the remaining analyses were then normalised to 100 %.

Trace element analyses of crystal phases and matrix glass were carried out at the University of Durham using a New Wave deep UV laser (193 nm solid state) coupled to an X-series 2 ICP-MS (inductively-coupled plasma mass spectrometer). Analyses were run using a 35 μm spot (for glass) or 50 μm spot (for crystals). The LA-ICP-MS data were internally normalized to ^{29}Si or ^{43}Ca from EPMA analyses. Abundances of single trace elements were calculated relative to a bracketing standard (NIST 612) which was analysed throughout the run under identical conditions. Precision and accuracies varied depending on the analytical conditions, but generally have <10% (2 s.d.) uncertainties (see Supplementary Data Electronic Appendix 1 for full details of precision and accuracy).

RESULTS

Whole-rock data

The whole rock data confirm that the samples typify the full range in magmatic compositions exposed on Ascension Island, from the least-evolved Green Mountain scoria sample (AI14-552; 47.7 wt % SiO_2 , 3.01 wt % Total Alkalis [TA]) through to the most evolved sample of 1094 kya (AI-94; Jicha *et al.*, 2013) felsic lava (72.3 wt % SiO_2 , 10.3 wt % TA; Fig. 3a, Table 2). When selected whole-rock trace element data are normalised to primitive mantle (Palme & O'Neill, 2003) felsic lava and pumice samples are clearly depleted in Sr, Ti and Ba relative to mafic lava and scoria samples (Fig. 3b). Felsic pumice and lavas are generally more enriched in incompatible trace elements than the mafic lavas and scoria (Fig. 3b).

The whole-rock data show increasing total alkalis, and decreasing CaO and MgO, with increasing SiO₂ (Fig. 4). Mafic lavas are typically more enriched in MgO, CaO and TiO₂ (Fig. 4a, c), and depleted in FeO, Na₂O, K₂O, Zr and Ba (Fig. 4b, d, f, Table 3), relative to felsic lavas. While having the textural characteristics of basaltic volcanism, samples of Letterbox ‘mafic’ lavas are in fact intermediate, with 55.8 – 57.6 wt % SiO₂, and 2.10 – 2.29 wt % MgO. Pumice and felsic lava samples have similar major and trace element concentrations (Figs 3, 4), as do mafic lavas and scoria (Figs 3, 4); thus there is no appreciable difference in whole-rock compositions between magmas erupted effusively or explosively (Figs 3, 4). Whilst there appear to be gaps within the MgO content (Fig. 4), these solely reflect the samples selected for study; when compared with a large published data set, no gaps in composition are observed for Ascension Island volcanics (Fig. 2c; Fig. 4 grey fields).

Petrology of Ascension lavas

Mafic and intermediate lavas studied are generally crystal poor, with less than 5% phenocrysts, apart from the samples from the South Coast (high Zr/Nb) lava with 18% and 40% phenocrysts in the two samples studied here (see Table 3, Fig. 5a, b). In the mafic and intermediate lava flows, phenocrysts (> 500 µm) are predominantly plagioclase feldspar (Fig. 5c, d), with minor olivine in some samples (Table 3, Fig. 5). Phenocryst phases in the crystal rich lavas (from the South Coast) are larger, up to 5mm, modal size 3mm, when compared with all other mafic and intermediate phases, where phenocrysts are generally < 1mm in diameter. The groundmass of all mafic and intermediate lavas studied here is microcrystalline, with no glass present. The groundmass consists of plagioclase feldspar, clinopyroxene, olivine and Fe-Ti oxides (Fig. 5a-d, Fig. 6) in decreasing order of abundance.

Felsic lava samples come from the (older) central felsic complex (AI14-103, AI15-621, AI-94; Fig. 1) and the (younger) eastern felsic complex (AI14-511, AI14-485, AI14-419, AI14-428). All felsic lavas are crystal poor, with <6% phenocrysts visible in hand sample (Table 3). Phenocrysts phases are dominantly ternary feldspars (plagioclase to alkali-feldspars, Fig. 7), with minor Fe-Ti oxides and aegirine-augite present as phenocryst phases in two samples (Table 3). Phenocrysts are always <3 mm diameter. In thin section, crystals are largely euhedral, and feldspar crystals often present as clots of 2-5 crystals (Fig. 5e-h; Fig. 6d, e). The groundmass is usually microcrystalline, consisting of ternary feldspar, cristobalite, interstitial aegirine-augite and Fe-Ti oxides in decreasing order of abundance (Table 3; Fig. 6d, e, f). A single felsic lava sample has a glassy matrix (AI14-419, the Letterbox felsic lava sample), which has SiO₂ concentrations between 71.2 and 74.0 wt % (Table 3; Fig. 11).

Mineral compositions of the mafic and intermediate lavas

Plagioclase feldspar is a dominant mineral phase in all mafic and intermediate lavas with compositions varying between An₃₇Ab₆₁Or₂ and An₈₂Ab₁₇Or₁ (Fig. 7). BSE images of feldspar crystals typically show faint oscillatory zoning (Fig. 6c) with the South Coast (high Zr/Nb) lavas having better developed zonation and resorbed cores (Fig. 6a, b). The lack of well-developed BSE image zonation patterns in the Sisters, Wideawakes and Letterbox feldspars (mafic lava fields, see Fig. 1 for name origins) is reflected in their major and trace element compositions, which show limited variations (Fig. 7, 8). The South Coast lavas exhibit some compositional variation between core and rims in their feldspar population (Figs 8c, 9a), with cores typically being less evolved than feldspar rims. Olivine compositions in the groundmass (or as phenocrysts in South Coast and Wideawakes samples) vary between Fo₄₉ – Fo₈₉. Where groundmass olivine can be identified separately from phenocrysts, groundmass olivines have higher CaO and lower MnO concentrations at any given value of

Fo number. Olivine crystals are faintly normally zoned, if they are zoned at all, with no evidence for resorbed cores in any samples studied (Figs 6a, b, 9b, 10).

No variation is seen in phenocryst compositions between the stratigraphically older and younger samples from the same geographic region. However, some variation in mineral compositions exists between different geographic regions, with differences in major and trace elements between geographic regions (Fig. 8a, c). Letterbox samples have more restricted feldspar and olivine compositions, representing the more-evolved end of the range in mineral compositions displayed by all mafic lavas (Fo 56 – 69; An 36 – 47; Fig. 8a; Figs 9, 10a, 10c), consistent with their whole-rock compositions (see Table 2). South Coast, Sisters and Wideawakes lavas generally contain more variable An-plagioclase (An 32 – 82; see Table 5, Figs 1, 8, 9), which has lower Sr concentrations (and extends to higher anorthite contents; Fig. 8a, c), and more variable olivine (that extends to less evolved compositions) than Letterbox (Fo49 – Fo89; Table 5, Fig. 1, 9, 10), consistent with their less evolved whole-rock compositions.

Mineral compositions of the felsic lavas

Ternary feldspar is the dominant mineral phase in all felsic lavas with compositions varying between $\text{An}_{20}\text{Ab}_{75}\text{Or}_5$ and $\text{Ab}_{70}\text{Or}_{30}$ (Fig. 7). BSE images of feldspar crystals from felsic lava samples are unzoned (Fig. 6d, e). However, some lava flows show core-rim-groundmass variations in feldspar compositions (see Fig. 8c and Supplementary Data Electronic Appendix 2), which is unresolvable in BSE images alone. In particular, sample AI14-485 (from the eastern felsic complex; Fig. 1) has systematically more evolved rims than cores, and more evolved groundmass than rims. Feldspar compositions of felsic lavas range from andesine ($\text{An}_{20}\text{Ab}_{75}\text{Or}_5$) through to anorthoclase ($\text{Ab}_{70}\text{Or}_{30}$; Fig. 7, Table 4), with the most evolved compositions ($\text{Ab}_{70}\text{Or}_{30}$) present in both the older and younger felsic samples (see Fig. 8b;

Supplementary Data Electronic Appendix 2). Most felsic feldspars (that are ternary) define a separate trend from the mafic and intermediate lava samples (with plagioclase feldspar only), having higher concentrations of Eu and Ba at any given Sr concentration (Fig. 8d). Aegirine-augite is present as a groundmass phase in all felsic lava samples studied here, with compositions between 0.5 – 12.1 wt % Na₂O and 0.1 – 6.2 wt % MgO. Aegirine-augite, typically < 500 µm (Fig. 11), commonly contains Fe-Ti oxide inclusions, and has higher Mn and lower Sr concentrations than the intermediate lavas (Fig. 11c), whilst the minor olivine (< 1%), present only in the Letterbox felsic lava, is Fo_{12.5} (see Supplementary Data Electronic Appendix 2).

The crystal compositions between samples of felsic lavas and samples of mafic to intermediate lavas do not overlap in their major elements. The samples from the younger eastern felsic complex (Fig. 1) have the greatest range in both feldspar (An₂₀Ab₇₅Or₅ – Ab₇₀Or₃₀) and clinopyroxene compositions (0.5 – 12.2 wt % Na₂O; Figs 8b, 11a, b; Tables 5, 7), while crystals within samples from the central felsic complex are typically more evolved; containing anorthoclase feldspar (An₇Ab₇₃Or₂₀ – Ab₇₀Or₃₀) and more aegirine-rich clinopyroxene (2.9 – 9.0 wt % Na₂O; Fig. 11a, b; Table 7).

Petrological variation in mafic pyroclastic deposits

Pyroclastic deposits are exposed all across the island and have compositions ranging from basalt to rhyolite, with no obvious Daly Gap when all published samples are considered (Daly, 1925; Figs 3, 4). The scoriaceous deposits studied here are crystal poor, with phenocrysts of plagioclase feldspar and minor olivine, clinopyroxene and Fe-Ti oxides. The Green Mountain scoria (AI14-552) is a relatively voluminous eruption, with widespread deposits originating from within the central felsic complex. Its key identifying feature is the presence of abundant white-cream plutonic lithic clasts. In thin section, juvenile scoria

typically contains plagioclase feldspar + olivine \pm clinopyroxene \pm Fe-Ti oxides. The groundmasses of the scoria clasts from these deposits have varying proportions of microlites (feldspar + olivine).

In BSE imagery, crystal phases are not zoned, and preserve euhedral crystal habits. Feldspar compositions overlap those of both the mafic and felsic lavas, ranging between $An_{14}Ab_{72}Or_{14}$ and $An_{84}Ab_{15}Or_1$. The Green Mountain scoria has the largest variation in feldspar compositions (AI14-552; Table 5), but there are no systematic differences in core and rim compositions of individual crystals (Fig. 8c, Table 5). Olivine, the other major phenocryst phase, overlaps compositionally with olivine in the mafic lavas, with Fo74 to Fo87 (Fig. 9b, 10b; Table 6) and also has no systematic difference in core and rim compositions from individual olivines (Fig. 10c). Matrix glass compositions are typical of mafic melts, with low SiO_2 (< 50 wt %) and high CaO (> 6 wt %), (Fig. 12; Table 8); the bulk scoria composition is slightly less-evolved (45.8 – 49.3 wt % SiO_2) than the NE Bay scoria (AI14-438, 49.0 – 52.4 wt % SiO_2).

Petrological variation in felsic pyroclastic deposits

Pumice clasts are typically crystal poor, with < 5% crystals. Ternary feldspar is the dominant crystal phase (oligoclase to anorthoclase composition \pm sanidine), with one ferromagnesian phase of either amphibole or fayalitic olivine, with minor magnetite \pm ilmenite \pm apatite, and rarely augitic clinopyroxene. One exception to this is the intermediate sample AI14-459 which has ~15% crystals, with large amphibole (up to 3 mm) phenocrysts. Crystal phases are not zoned in BSE, and preserve euhedral crystal habits. Groundmass is typically glassy, with varying amount of feldspar microlites.

Feldspar compositions from these pumice fall deposits overlap and straddle those from the evolved effusive eruptions (Fig. 7; Table 4): with compositions ranging between

$\text{An}_{51}\text{Ab}_{47}\text{Or}_2$ and $\text{An}_{0.5}\text{Ab}_{58.5}\text{Or}_{41}$. Some eruptions have relatively restricted feldspar compositions (e.g. AI14-488: $\text{An}_{0.5}\text{Ab}_{65.5}\text{Or}_{34}$ – $\text{An}_1\text{Ab}_{69}\text{Or}_{30}$) whereas others extend over wide ranges (e.g. AI14-435: $\text{An}_2\text{Ab}_{73}\text{Or}_{25}$ – $\text{An}_{18}\text{Ab}_{76}\text{Or}_6$). In trace elements, the felsic pyroclastic feldspars plot within the higher- and lower-Eu trend (Fig. 8d). No clear core-rim relationships were found in feldspar compositions: only one pumice fall deposit in Middleton's Valley (AI14-459) has slightly less-evolved cores relative to rim compositions (cores: $\text{An}_{51}\text{Ab}_{47}\text{Or}_2$ – $\text{An}_{20}\text{Ab}_{74}\text{Or}_6$; rims $\text{An}_{43}\text{Ab}_{54}\text{Or}_2$ – $\text{An}_{20}\text{Ab}_{74}\text{Or}_6$). This comparatively crystal-rich sample (see Table 3) also bridges the divide between our felsic and mafic lava feldspar populations. Fosterite content in olivines (Fo1 – 57) from felsic pyroclastic samples mirrors the relationships between pyroclastic and effusive lava feldspars- intersecting with and extending the range in compositions of mafic lava sourced olivines (Fig. 10b; Table 6). Again, no differences between core and rim compositions are observed in olivine from all pyroclastic samples (Fig. 10c).

Glass compositions of felsic pyroclastic deposits range from ~ 66 wt % to 75 wt % SiO_2 (Fig. 12; Table 8). All sampled pyroclastic deposits have relatively homogenous glass compositions, with the one exception being the glass from the compositionally-zoned fall deposit, previously described in Chamberlain *et al.* (2016; Fig. 12a). In detail, individual sample variation in trace elements shows up to a four-fold variation in elements compatible in feldspar (Ba, Sr; Fig. 12b). However, limited variations in source-related trace elements (such as Th/U ratio; Fig. 12c) are evident between samples, where variation within a single sample is of the same magnitude or greater than variations between samples.

Intensive variables

Where available, two co-existing oxides (magnetite and ilmenite) were analysed and Fe-Ti oxide thermometry of Ghiorso & Evans (2008) was applied (if the pairs passed the

equilibrium test of Bacon & Hirschman, 1988). Iron-titanium oxide derived temperatures range from 932 °C to 1037 °C for the mafic lavas (Table 8). Oxygen fugacity varies between -0.45 log units relative to the Nickel-Nickel Oxide (Δ NNO) buffer to $+0.05$ log units Δ NNO. Felsic lavas and pyroclastic samples yield Fe-Ti oxide temperatures ranging from 850 °C to 960 °C, and fO_2 ranging from -0.5 log units Δ NNO to -2.3 log units Δ NNO (Table 8).

Plagioclase-melt thermometry (Putirka, 2008) and alkali feldspar-melt thermometry (Putirka, 2008) was applied to all samples where equilibrium between feldspars and melt could be established (Putirka, 2008). Pressures of 330 MPa were assumed for mafic samples, as this is consistent with equilibration at the base of the crust, (Klingelhöfer *et al.*, 2001) and pressures of 250 MPa were used for felsic samples, based on melt inclusion entrapment pressures modelled from samples of a zoned fall deposit on Ascension Island (Chamberlain *et al.*, 2016). This modelling yielded temperatures within a similar range (but often higher) to that of the Fe-Ti oxide thermometry (Table 8), with modelled temperatures ranging between 772 °C and 1034 °C for felsic samples, and between 1093 °C and 1174 °C for mafic samples (Table 8). Although a specific pressure was assumed, testing demonstrated that the pressure effect is minimal, with less than 10 °C variation in estimated temperatures with > 200 MPa variation in assumed pressures.

Using measured alkali feldspar-melt compositions and temperatures modelled from plagioclase-melt thermometry, the alkali feldspar-melt hygrometer of Mollo *et al.* (2015) was also applied (see Table 8 for summarised results, full results in Supplementary Data Electronic Appendix 2). Calculated water concentrations are high (average concentrations for the felsic units between 4.66 wt % and 8.12 wt %, Table 8). Modelled water contents associated with the felsic lava and dome samples have consistently lower water concentrations than the explosively erupted samples. These high concentrations of water in explosive felsic samples are similar to those measured in Ascension Island melt inclusions

(Chamberlain *et al.*, 2016) and with the high loss on ignition from felsic pyroclastic samples measured during XRF analyses (see Supplementary Data Electronic Appendix 2 for full XRF results).

DISCUSSION

Origin of compositional variations in Ascension Island magmas

A range in whole-rock and crystal compositions are evident in Ascension Island samples, with no clear differences observed between effusively erupted lava samples and explosively erupted pumice and scoria samples (Figs 4, 7a). When considered alone, the variations in whole-rock chemistry presented here (Fig. 4) do not give reason to disagree with previous whole-rock studies of Ascension Island, which have suggested that fractional crystallisation is the dominant mechanism for producing evolved melts (e.g. Harris, 1983; Kar *et al.*, 1998; Jicha *et al.*, 2013; Chamberlain *et al.*, 2016), evidenced by the continuous trend in major and trace element concentrations (Figs 3, 4; Weaver *et al.*, 1996; Kar *et al.*, 1998; Jicha *et al.*, 2013), and the lack of whole-rock radiogenic isotopic ratio variation with major element concentrations (Fig. 2d; Weaver *et al.*, 1996; Kar *et al.*, 1998; Paulick *et al.*, 2010).

Partial melting of mafic material is another process through which felsic melts have been proposed to be generated at ocean island volcanoes (e.g. Borhson & Reid, 1997; Sverrisdottir, 2007; Carley *et al.*, 2011; Kuritani *et al.*, 2011). Unlike other ocean islands, there is no evidence for divergence in Nd isotopic ratios between mafic and felsic melts (Kar *et al.*, 1998), and major and trace elements vary co-linearly (Fig. 2b; Kar *et al.*, 1998; Jicha *et al.*, 2013), which previous studies suggest is not supportive of a partial melting origin for evolved melts at Ascension. Some minor assimilation and contamination has been inferred to be partly responsible for the radiogenic Sr isotopic compositions of more felsic melts (Kar *et al.*, 1998), but this cannot be quantified based on the new data presented here, and it is noted

that none of the earlier samples were acid leached prior to analysis (cf. Davidson *et al.*, 1997). At other volcanic systems where partial melting has been shown to be a significant driver for the production of evolved magmas, magmatic compositions can be bimodal, with few erupted magmas of intermediate composition (e.g. Charlier *et al.*, 2013, Meade *et al.*, 2014), which is not observed at Ascension (Figs 3, 4). However, small degree direct partial melting of a seawater-altered basaltic/gabbroic component cannot be ruled out with our new data set for Ascension (cf. Kar *et al.*, 1998), and may be responsible for some of the variation in $^{87}\text{Sr}/^{86}\text{Sr}$ isotopic ratios (Fig. 2a).

Magma mixing between mafic and felsic magmas to produce the intermediate rocks could be responsible for the continuum in whole-rock compositions at Ascension (Fig. 3), yet non-linear variations in major and trace elements in both whole-rocks (especially in TiO_2 , K_2O and Zr, Fig. 4) and crystal phases (Figs 8d, 10d) suggest that this is unlikely. Similarly, crystal compositions form coherent trends within individual samples, with no evidence for distinct populations (cf. Geist *et al.*, 1995; Troll & Schminke, 2002; Figs 8 – 11) that could represent growth in different magmas. Petrographic data shows no evidence of magma mixing, therefore fractional crystallisation is hypothesised to be the main mechanism for generation of felsic melts at Ascension Island, in agreement with previous authors (cf. Kar *et al.*, 1998; Jicha *et al.*, 2013).

To test the fractional crystallisation hypothesis further, MELTS modelling of isobaric liquid lines of descent (Gualda & Ghiorso, 2015) from the least evolved sample (AI14-438, see Table 1) has been undertaken at a range of pressures, from 330 MPa (the base of the crust, Klingelhöfer *et al.*, 2001) to 90 MPa (~ 3.5 km depth), as well as an isothermal decompression model from 90 MPa to 1MPa (Figs 13, 14). An initial starting composition based on AI14-438 was used, with an assumed water concentration of 0.5 wt % H_2O , and $f\text{O}_2$ at the NNO-buffer based on Fe-Ti oxide thermometry (Table 8) and analyses of nearby MAR

glasses (Almeev *et al.*, 2008) which tap a mixed enriched Ascension Island-type source and a depleted high ϵ_{Hf} mantle (Paulick *et al.*, 2010). It has been shown that oxygen fugacity is not solely fractionation dependent at Ascension Island (Chamberlain *et al.*, 2016) and this one-step MELTS modelling does not properly reflect the fractionating phases at the more evolved end. Thus, at $T < 950^\circ\text{C}$ the composition of AI15-621 was used, the least evolved of the felsic lava samples, with an assumed water concentration of (5.1 wt % H_2O) from feldspar-melt hygrometry, and $f\text{O}_2 -1.5 \Delta\text{NNO}$ from Fe-Ti oxide thermometry (Table 8).

The modelled liquid lines of descent of this two-step MELTS modelling reproduce the observed variations in whole-rock composition (Fig. 13), with the models run at higher pressure (250 MPa or greater) having a better fit for MgO and CaO concentrations (Fig. 13b, c), suggesting fractionation at depths of more than 7 km. At the more evolved compositions (>68 wt % SiO_2), fractionation at 170 MPa better reproduces the more evolved compositions of Ascension Island magmas (Fig. 13a). Whilst isobaric fractionation is unlikely to occur at Ascension Island, the MELTS modelling shows that simple fractional crystallisation can replicate the observed variations in whole-rock composition, when oxygen fugacity is controlled to represent that measured in Ascension Island magmas. Similarly, modelled increases in H_2O with increasing SiO_2 support the modelled high melt H_2O concentrations from feldspar-melt hygrometry (Table 8), especially at higher pressures of evolution (Fig. 13d).

Fractional crystallisation in mafic and intermediate magmas

Fractional crystallisation, as modelled by MELTS, has demonstrated that the observed whole-rock compositional range within the Ascension Island magmatic suite can be reproduced by this process. For the mafic and intermediate magmas, the crystal compositions measured overlap well with the modelled crystallising phases from MELTS (Fig. 14), and up to 70%

total fractionation has occurred to produce the most evolved intermediate magmas (Fig. 13). Whilst MELTS details proportions of phases fractionating, previous studies have demonstrated some limitations on the model's ability accurately to predict crystallisation of water-bearing phases (Gualda *et al.*, 2012), clinopyroxene (Fowler & Spera, 2010) and apatite (Rooney *et al.*, 2012). Therefore, to yield further insights into the proportions of phases crystallising, least-squares modelling of the major elements has been undertaken, constrained by using only phases observed in samples of Ascension Island volcanic rocks.

Major element least-squares modelling was carried out using Petrograph (Petrelli *et al.*, 2005, built on the least-squares modelling of Stormer & Nicholls, 1978), and to include entrainment where appropriate (cf. Kar *et al.*, 1998, Supplementary Data Appendix 3). A comparison of the phases crystallising at each modelled stage between MELTS and Petrograph can be seen in Appendix 3. Two stages of evolution are considered initially, to attempt to reproduce the variations in mafic to intermediate whole-rock compositions (Fig. 3): Stage (1) from the NE Bay Scoria (the most primitive basalt; AI14-438) to the Wideawakes (an intermediate Zr/Nb basalt marking the inflection in MgO vs TiO₂, Fig 4c; AI-445); Stage (2) Wideawakes (AI14-445) to Letterbox (an intermediate lava; AI14-423). In both stages, the compositions of plagioclase feldspar, olivine, clinopyroxene, ilmenite and magnetite measured in the parent sample were used. Apatite was also used as an accessory phase, given its presence as inclusions in mineral phases and the variation in P₂O₅ evident in the whole-rock data (Table 2; full details of modelling conditions see Supplementary Data Appendix 3). Whilst this modelling is limited by the assumption of uniform compositions of the fractionating phases, and has no pressure or temperature dependence, it provides a first order constraint on the modal fractionating assemblage, provided that the sum of the squared residuals is < 2 (Stormer & Nicholls, 1978). Stage 1 fractionation modelling (sum of squared residuals [SSR] 0.25) suggests that ~ 8% fractionation of an assemblage dominated by

plagioclase feldspar with subordinate olivine and apatite, coupled with the minor entrainment (4%) of clinopyroxene and two oxides, could produce the compositions of AI-445. The second stage of modelling (SSR 0.05), to produce the intermediate Letterbox magmas, suggests a further 56% fractionation (0.4 melt fraction remaining) of an assemblage dominated by feldspar and clinopyroxene, with minor olivine, magnetite, ilmenite and apatite (See Supplementary Data Appendix 3 for graphic representation and comparison with modelled MELTS fractionating phases).

These modelled fractionating assemblages have been further tested using published distribution coefficients for Rb, Sr, Y, Zr, Nb and Ba in the fractionating phases (Fig. 15, full details and references for the distribution coefficients used are given in Supplementary Data Appendix 3). Generally fractional crystallisation (excluding any accumulation) can reproduce the observed variations in Rb, Nb, Ba and Zr, with a poorer agreement with Sr and Y data (Fig. 15 and Supplementary Data Appendix 3) for the variation observed in the mafic magmas.

Felsic magma evolution

Felsic magma evolution through closed system fractional crystallisation, modelled by MELTS, is shown to reproduce well the major elements of the whole-rock data for Ascension, for most elements (Fig. 13), and that pressure of fractionation has a significant effect on total alkalis (Fig. 13a), reflecting the pressure-sensitivity of feldspar crystallisation (Fig. 14a). Fractionating assemblages again reproduce well the measured compositions of feldspar, olivine and clinopyroxene. In the more-evolved lavas, growth of low-pressure phases (evidenced by feldspars with ~4 – 6 wt % K₂O and Na-rich clinopyroxenes, Fig. 14a, c) reflect growth at a range of pressures (cf. isothermal decompression crystal compositions from MELTS modelling; Fig. 14) which are not observed in equivalent explosive deposits.

Again, to supplement the MELTS modelling, major element least-squares modelling was carried out using Petrograph (Petrelli *et al.*, 2005; after Stormer & Nicholls, 1978). Two further stages of evolution were considered, to attempt to reproduce the trends observed in whole-rock concentrations (Fig. 3): Stage (3) Letterbox (AI14-423) to Devils Riding School (representative of the trachytic lavas on Ascension, Fig 3; AI15-621) and Stage (4) Devils Riding School (AI15-621) to Middleton's Ridge (most-evolved rhyolite, AI-94). In both stages, the compositions of feldspars (plagioclase and ternary feldspar), olivine, clinopyroxene, ilmenite and magnetite measured in the parent sample were used. Apatite was also used as an accessory phase, given its presence as inclusions in mineral phases and the variation in P_2O_5 evident in the whole-rock data (Table 2; full details of modelling conditions given in Supplementary Data Appendix 3).

Stage 3 (SSR 1.23) requires a further 60% fractionation (0.16 melt fraction remaining from initial mafic starting sample) of an assemblage again dominated by plagioclase feldspar, with subordinate clinopyroxene, apatite, ilmenite, and minor entrainment of magnetite (1%). Contrastingly, MELTS modelling suggests both biotite and orthopyroxene should begin to fractionate (neither of which have been observed on Ascension Island, Supplementary Data Appendix 3). Stage 4 (SSR 0.08) shows a clear change in fractionating assemblage with ternary feldspar dominating the fractionating assemblage with clinopyroxene and magnetite, and requiring a further 57% fractionation (0.07 melt fraction remaining, in agreement with MELTS modelling of liquid lines of descent: 0.06 melt fraction remaining, Fig. 13). Minor accumulation (4%) of fayalite, ilmenite and apatite contributes to the evolution of the felsic magmas (see Supplementary Data Appendix 3). These inferred fractionating phases are in good agreement with the observed crystal phases present in Ascension samples with feldspar being the dominant crystal phase present, with minor fayalitic olivine or clinopyroxene, unlike MELTS modelling which again fails to accurately reproduce the observed mineral

phases, with the suggested presence of leucite and orthopyroxene (Table 3, Supplementary Data Appendix 3).

Trace element modelling of the proposed fractionating assemblages was undertaken for Stages 3 and 4, again excluding any accumulation of phases. The results of this modelling show that Ba is successfully modelled by this fractionating assemblage, with moderate but less consistent results for modelled *versus* measured Sr and Nb (Fig. 15, Supplementary Data Appendix 3). There is poor agreement between modelled and measured Zr, Rb and Y (Fig. 15, Appendix 3). Zircon is observed in the most evolved samples, but fractionation of this phase has not been modelled as the proportions are challenging to quantify using major element modelling, although it could be the cause of the variations between observed and modelled concentrations of Zr and Y in the felsic magmas of Ascension. We note that accumulation or fractionation of minor phases, whilst not significant in terms of the major element evolution of the felsic melts, can significantly affect the trace element compositions of melts. With a K_d of ~ 40 in rhyolitic apatites (Pearce & Norry, 1979), Y concentrations will be significantly affected by even minor amounts of fractionation of this phase.

The role of ascent rate and oxygen fugacity

Use of MELTS modelling to yield crystal compositions has highlighted the role of crystal growth in the upper crust during ascent in the presence or absence of phases in the felsic magmas. Moderate 4 – 6 wt % K_2O feldspar and aegirine-augite are only found in felsic lavas; in felsic pyroclastic samples no feldspar has 4 – 6 wt % K_2O and fayalite is the common ‘mafic’ phase (Fig. 10b)- rare clinopyroxene is augitic in composition, and reflects fractionation at pressures ≥ 90 MPa (Fig. 14c). Pyroclastic samples have high, modelled water concentrations (Table 8) perhaps reflective of higher pressure storage (Fig. 13d, cf. Di Matteo *et al.*, 2004; Brenna *et al.*, 2014). Combining the lack of chemical zonation (Figs 9c,

10c), the euhedral nature of the phenocryst phases (Fig. 6), and no low-P phases forming (cf. Fig. 14c), ascent rates for pyroclastic magmas, fractionating at high pressures (≥ 250 MPa, c.f. Fig. 13) is likely to be rapid and warrants further comparison with their effusive counterparts.

In other alkaline systems it has been shown that variations in fO_2 at constant temperatures can result in variable phase assemblages (White *et al.*, 2009; Markl *et al.*, 2010). Given the large variation in calculated fO_2 within Ascension Island magmas (Table 8), some of the small variation around liquid lines of descent, and mismatch between the MELTS-modelled *versus* observed phases, may stem from variable phase crystallisation at differing fO_2 conditions, as well as variations in ascent rate and depth to magma storage regions within the lower crust.

Spatial and temporal variations in magmatism at Ascension Island

Temporal and spatial variation of mafic magmas

Whole-rock major and trace element data and crystal compositions show little variation between samples of older and younger lavas (Table 2, Fig. 4) from the same eruptive centres, suggesting that the mode of mafic magma generation and ascent has been relatively constant for the subaerial (and exposed) history of Ascension Island. This is in agreement with previous whole-rock isotopic data, which shows no clear variation in the subaerial edifice of Sr, Nd or Pb isotopic ratios over time, indicative of source characteristics (Weaver *et al.*, 1996; Kar, 1997; Paulick *et al.* 2010; Jicha *et al.*, 2013). While there is no temporal variation in the composition of mafic subaerial magmas erupted on Ascension, there are significant spatial differences in the phenocryst percentages, whole-rock compositions, and crystal compositions, depending on the location of the eruptive centre (detailed in Table 1, Table 3, and Figs 4, 8, 10). South Coast lavas have the highest crystal contents ($>17\%$) and the least-

evolved crystal compositions (down to An₈₂, and Fo₈₇; Figs 8, 10), whereas the Letterbox samples from the SE of the island are intermediate in composition, contain clinopyroxene as a minor component (instead of olivine; Table 3), and have more restricted feldspar compositions.

Origin of the crystal cargo

Given the marked differences in crystallinity between the South Coast lavas (AI14-522 and AI14-514; Table 1) and the other mafic to intermediate lavas (Table 3), modelling of plagioclase and olivine equilibrium compositions, based on the whole-rock compositions at an assumed temperature and pressure, following the method of Price *et al.* (2012), was undertaken (Fig. 9). The range in olivine Mg# from different eruptive centres (Fig. 9) shows that not all of the olivine crystal cargo is modelled to be in equilibrium with the melt in which it is erupted (Fig. 9b). Rim analyses are just as likely to be in disequilibrium with the whole-rock compositions as core analyses. This range in olivine Mg# shows that some crystals are not phenocrystic, despite the lack of significant overgrowths and the crystals mostly having a euhedral to subhedral habit (Fig. 6).

Similarly, plagioclase feldspar compositions are not in equilibrium with their whole-rock compositions (Fig. 9a) and yet only feldspars from the South Coast lavas display reaction rims and anhedral cores (Fig. 6b). Whilst the calculation of equilibrium plagioclase compositions (following the method of Panjasawatwong *et al.*, 1995) is only calibrated for plagioclase feldspar compositions (and not in alkaline systems such as Ascension), and thus could be a potential reason why feldspars are in apparent disequilibrium, single samples preserve a wide variation in An content in the feldspars, showing that irrespective of the modelled equilibrium conditions, significant amounts of feldspar crystals will not be in equilibrium with their host-rock composition.

Mafic lavas, excluding those from the South Coast group, are clearly in chemical disequilibrium with their feldspars, with less variation from the calculated equilibrium composition for olivines (Fig. 9). Densities of the mafic magmas were calculated following the method of Bottinga & Weill (1970), at pressure of 330 MPa (equivalent to the base of the crust (Klingelhöfer *et al.*, 2001) using measured whole-rock compositions and a water concentration of 0.5 wt %. Densities of mafic magmas are on the order of 2.7 g/cm³, remarkably similar to that of plagioclase feldspar (2.6 – 2.7 g/cm³, Scoates, 2000; Ghiorso & Gualda, 2015), yet less dense than olivine and clinopyroxene, (~3.6 g/cm³ and ~3.2 g/cm³ respectively, Scoates, 2000; Ghiorso & Gualda, 2015). Thus, fractionating feldspar in a zone of magma storage will not sink, and instead may form lateral mushy cumulates as the magma evolves, whereas olivine and clinopyroxene have bigger density differences with the mafic magmas, and thus can sink more effectively. As the mafic magma reaches eruptible conditions, either due to concentration of volatiles within the magma (e.g. Stock *et al.*, 2016), tectonic destabilisation of the system (e.g. Allan *et al.*, 2012), or through gas injection (e.g. Caricchi *et al.*, 2018), the mafic magma rapidly incorporates these lateral mushy feldspar antecrysts, producing the wide range in feldspar compositions found within single eruptions, that are in disequilibrium with their whole-rock composition, yet native to the magmatic system (Fig. 9a, 14a). The timescale of incorporation of these antecrystic crystals prior to eruption must be short, as no zonation is observed (see Figs. 8 – 10), and the feldspars generally retain their euhedral appearance (Figs 5, 6). Similarly, the mushy storage regions in which the feldspars and mafic phases are forming are transient; no evidence is preserved for long-lived melt-dominant magma storage regions for mafic to intermediate magmas, with no evidence for incorporated crystals seeing more than one ‘triggering’ event (cf. Kahl *et al.*, 2013).

Role of crystal entrainment in mafic to intermediate magma genesis: Excluding the South Coast group lavas, all other mafic and intermediate lavas have crystallinities less than 5% (Table 3), with limited evidence for chemical zonation (Fig. 10c) and euhedral crystal habits (Fig. 4, 6), thus incorporation of mushy antecrysts (which are subsequently resorbed) appears unlikely to constitute more than 5% (total rock crystallinity) of the rock volume. The similarities in antecrystic and phenocrystic crystal cargo in Ascension Island lavas make assessing the proportions of assimilated material challenging, as incorporation of these antecrysts may merely shift the whole-rock compositions along the modelled liquid line of descent. This has implications for modelling the total amount of fractional crystallisation responsible for individual mafic and intermediate magmas, thus these estimates of degree of fractional crystallisation from both MELTS and the least-squares modelling must be treated with caution.

Lavas in the South Coast group have relatively high crystallinity compared with other mafic and intermediate lavas (Table 3), with crystals that show the most zoning in BSE imagery and major and trace element analyses (Fig. 6, 8), and feldspars that lie furthest from the modelled equilibrium compositions (Fig. 9). These South Coast lavas are also observed to contain significant proportions of plutonic lithic clasts (ranging from gabbro to syenite, Roedder & Coombs, 1967; Harris *et al.*, 1982; Harris, 1983; Webster & Rebbert, 2001). These observations suggest that the range in compositions of feldspar and olivines found in South Coast lavas is the result of incorporation of large amounts crystals from other sources, as antecrysts or xenocrysts (Charlier *et al.*, 2005). Potential sources of contaminant crystals are oceanic crust (thus crystals are xenocrystic), plutonic bodies related to Ascension Island magmatism (thus antecrysts), or from a mushy, not yet solid, fractionated crystal residue (also antecrysts, as in the other mafic to intermediate lavas, above). Few analyses of crystals from the abundant lithic clasts exist, however feldspar compositions from gabbros overlap those

found in the mafic lavas (Harris, 1983) and isotopic data suggests a cogenetic origin for gabbros and mafic lavas (Weis *et al.*, 1987). Contrastingly, ocean crust feldspars define a lower K₂O trend than alkaline-magmatism-sourced feldspars when plotted against An content (Davis *et al.*, 2007). No difference is seen in the feldspar and olivine compositions of the South Coast lavas (Fig. 7 – 10), suggesting that incorporated crystals are antecrystic (and not xenocrystic, see representative compositions of Mid-Atlantic Ridge feldspar crystals in Fig. 8b) in origin. No evidence is seen in crystal compositions or textures for mixing with a chemically distinct magma, thus mechanical incorporation of antecrystic plutonic material (e.g. Humphreys *et al.*, 2009) is our favoured method by which these materials are included within the South Coast lavas, on top of the ‘background’ accumulation of mushy antecrystic material similar to the other mafic and intermediate lavas.

South coast lavas are the only samples studied here which show overgrowths on feldspars (Fig. 6b), glomerocrystic textures (Fig. 5b) and increased crystallinity, suggestive of higher degrees of antecryst incorporation. The relative importance of antecrysts in south coast lavas could be due to these south coast magmas having a greater ability to erode these deep mafic plutonic bodies upon ascent, or that that these deep mafic plutonic bodies are only present in the source and ascent region of the crust through which the south coast lavas travel prior to eruption. A magma’s ability to mechanically disaggregate any lithic fragment is dependent upon its enthalpy and composition (Glazner, 2007). The variations in whole-rock compositions between south coast lavas and other mafic lavas is not significant (Fig. 4), thus only variations in temperature could change the magmas ability to erode and disaggregate the plutonic lithic fragments. Modelled feldspar-melt temperatures are similar across the suite of mafic lavas (Table 8) and so it seems unlikely that increased antecryst incorporation is due to an increased ability of south coast magmas to erode plutonic lithic fragments. Instead, the increased proportion of antecrysts in south coast lavas is suggested to reflect an increased

presence of mafic plutonic rocks at depth in this region. These plutonic rocks are anteliths, related to Ascension Island magma generation and not oceanic crust plutonic rocks (Fig. 8b), and highlight the lateral variability in plutonic or mushy regions within the Ascension Island crust.

Crustal control on the location of felsic eruptive centres

Eruptions of felsic magma occurred from two main centres: the older central felsic complex, and the younger eastern felsic complex, with mafic magmas erupted around the peripheries of these centres (Fig. 1; Jicha *et al.*, 2013). In these regions, felsic magmas - erupted as lavas and pyroclastics - are the dominant magma type. Spatial separation of mafic and felsic lavas has been seen at other ocean islands (both active and extinct), and has been suggested to be a result of crustal structure inhibiting the ascent of more dense mafic magmas in the felsic complexes (e.g. Mahood & Hildreth, 1983; Druitt *et al.*, 1995; Carracedo *et al.*, 2007; Brenna *et al.*, 2015).

Active-source tomography reveals an area of elevated seismic velocities in the core of the island, at 6.5 km depth beneath the felsic complexes (Evangelidis *et al.*, 2004). This was interpreted to represent a single crystallised magma body, supported by the presence of plutonic lithic clasts in the erupted products (e.g. Roedder & Coombs, 1967; Harris, 1986; Weis *et al.*, 1987; Hobson, 2001; Webster & Rebbert, 2001). This central core of nested plutonic rocks (of gabbroic through to granitic compositions – Roedder & Coombs, 1967) under the felsic complexes could inhibit the ascent of almost all mafic magmas in these regions.

The presence of plutonic rocks in ocean island crust has long been known to affect the evolution of magmas prior to eruption—the volcanic islands of Terceira (Mungall & Martin, 1995) and Oki-Dōzen (Brenna *et al.*, 2015), among others, have evidence for central felsic

complexes (both as plutonic rocks, and as storage regions for felsic volcanic eruptions) which inhibit the eruption of mafic magmas. Ascension Island has a modelled growth rate of 0.4 km/Myr (Minshull *et al.*, 2010), which is significantly lower even than post-shield Hawaii (0.9 km/Myr, Minshull *et al.*, 2010 and references therein), and dramatically lower than shield stage Mauna Kea (8.6km/Myr, Minshull *et al.*, 2010 and references therein). Therefore we suggest that this ‘filtering’ of mafic magmas and spatial segregation of mafic and felsic eruptive centres could be a result of low rates of magmatic flux. If magmatic flux is higher, this could destabilise the central felsic systems, and mafic and felsic magmas would no longer show such clear spatial separation, and mixing textures would be much more dominant, such as those observed in Tenerife (Sliwinski *et al.*, 2015) or Iceland (Carley *et al.*, 2011), where mafic and felsic magmas are still produced, but with less clear spatial separation and an increased role of partial melting of crustal material than that inferred at Ascension.

We suggest that multiple plutonic bodies representative of multiple ephemeral magma reservoirs, rather than a single magma body, are necessary to generate the range in compositions seen on Ascension Island, as there is no evidence from crystal compositions for repeated use of a single magma storage region which is repeatedly rejuvenated (cf. Kahl *et al.*, 2013). This observation suggests that the ‘plutonic body’ identified seismically (Evangelidis *et al.*, 2004) beneath Ascension is a series of smaller-volume, nested plutonic bodies which cannot be resolved seismically from a single large body of the same dimensions (Bauer *et al.*, 2003).

The presence of plutonic lithic clasts in pyroclastic fall deposits on Ascension Island (including some of the oldest fall units on the island, Hobson, 2001), combined with the rhyolitic nature of the oldest-dated subaerial lava (Jicha *et al.*, 2013), implies that the plutonic complex was established well before the beginning of the subaerial phase of Ascension

Island's volcanic history. While the felsic plutonic and volcanic rocks share an apparently common origin (with similar isotopic characteristics, Weis *et al.*, 1987, and following the same liquid line of descent, Harris *et al.*, 1982) the timing of pluton formation must pre-date the earliest subaerial eruptions on the island (1094 ka; Jicha *et al.*, 2013), and could relate to the more voluminous submarine volcanism that began ~5 – 6 Myr ago (Minshull *et al.*, 2010; Paulick *et al.*, 2010).

The magmatic plumbing system

Here we combine our new results with all previously published data to present a model for the magmatic plumbing system underlying Ascension Island (Fig. 16) during the subaerial phase of activity from ~1 Ma to the present. The key features of the model are as follows:

- 1) A zone of melt extraction, from which all Ascension Island volcanism is sourced, by varying degrees of partial melting (Fig. 16; Paulick *et al.*, 2010; Jicha *et al.*, 2013). This melt extraction zone is geochemically distinct from the mantle melting responsible for the significantly larger volume submarine volcanism of Ascension which was active from ~5-6 Ma to ~3 Ma (Minshull *et al.*, 2010; Paulick *et al.*, 2010).
- 2) Heterogeneity in the lower crust affects the ascent and incorporation of antecrysts in basaltic melts. The variably over-thickened layer 3 (lower crust) presently underlying Ascension Island (Klingelhöfer *et al.*, 2001) likely formed during the large volume, on-axis volcanism which built the submarine edifice (Minshull *et al.*, 2010). We suggest that the over-thickening of layer 3 (represented mainly by mafic plutonic lithic clasts, not the nested felsic plutonic lithic clasts) is most significant underneath the vents for the South Coast lavas (AI14-514, AI14-522). South Coast lavas contain many crystals that are not in equilibrium with their whole-rock compositions (Fig. 9), suggesting that these magmas have mechanically incorporated large amounts of

antecrystic feldspar and olivine, shortly prior to eruption. This spatial heterogeneity in the deep mafic plutonic rocks is reflected in the proportions of antecrysts incorporated during the ascent of mafic magmas.

- 3) A central nested region of small discrete plutonic bodies of varying composition (with a higher proportion of felsic bodies), which forces the majority of ascending mafic magmas to stall and fractionate until they reach a level where their buoyancy has increased enough to allow them to ascend further. This is supported by the felsic plutonic lithic clasts within the Green Mountain scoria, erupted in the central felsic complex, and by mechanically incorporated plutonic lithic fragments in many felsic pyroclastic deposits (Fig. 16).
- 4) Felsic magma evolution occurs only in the lower crust at pressures greater than 170 MPa (Fig. 13). No evidence is seen for magmatic stalling (and subsequent eruption) of felsic melts stored at pressures less than 170 MPa. The only modelled entrapment pressures from melt inclusions from a zoned fall deposit on Ascension Island showed that crystals grew in a storage region at 250 MPa (Chamberlain *et al.*, 2016), with melt inclusions having up to 4 wt % H₂O. This is in agreement with modelled entrapment pressures from felsic plutonic bodies being between 200 and 300 MPa (or 6.8 – 10.2 km, assuming a crustal density of 3000 kgm⁻³; Webster & Rebbert, 2001). The modelled high water concentrations of melts from which feldspars have grown (Table 8) could support this storage and evolution within the lower crust (or Layer 3 of Klingelhöfer *et al.*, 2001; Figs 13, 16). Lower crustal storage means that any unrest signals will be harder to resolve, and has implications for the methods implemented to monitor future volcanic unrest on Ascension Island.
- 5) Magmas were erupted as discrete batches, with no evidence for long-lived storage, or for crystal recycling between eruptions in a mushy or melt-dominant magma storage

region (cf. Kahl *et al.*, 2013). Magma mixing is therefore not an eruptive trigger.

Instead, triggers could be internal (due to volatile over-pressure), or from external tectonic changes, which again presents challenges for monitoring potential future volcanic unrest at Ascension Island.

- 6) The magmas that fed explosive and effusive felsic eruptions exhibit differences in the presence or absence of low-pressure phases (Fig. 14), perhaps suggestive of variation in the location of their storage regions and ascent rates, and warrants further investigation. However, fractional crystallisation (with minor crystal entrainment) of predominantly feldspars induced by stalling (at varying depths) in the nested (more felsic) plutonic region, remains the dominant evolutionary process for all felsic magmas, irrespective of the eruptive style.

Implications for the generation of felsic magmas on ocean islands

The petrogenetic processes responsible for the generation of felsic magmas in ocean island volcanoes built on thin oceanic crust have long been debated. Many authors have suggested that felsic magma production at ocean island volcanoes could be a proxy for the initiation of continental crust formation in the Archean (e.g., Gazel *et al.*, 2014; Mancini *et al.*, 2015).

While the low growth rates of Ascension Island (Minshull *et al.*, 2010) negate its use in understanding Archean felsic magma genesis, the dominance of fractional crystallisation in the generation of felsic magmas, with little evidence for magma mixing, is unusual when compared with other ocean island volcanoes (e.g., the Canary Islands and Iceland: e.g.

Borhson & Reid 1997; Caroff *et al.*, 1999; Sverrisdottir, 2007; Carley *et al.*, 2011; Longpré *et al.*, 2014).

Open versus closed system evolution

The new data presented here suggest that evolution of Ascension Island magmas is dominated by simple crystal fractionation in a relatively closed system of short-lived, discrete, magma storage regions, and supports the conclusions of previous workers (Harris *et al.*, 1982; Kar *et al.*, 1998; Webster & Rebbert, 2001; Jicha *et al.*, 2013; Chamberlain *et al.*, 2016). This is contrary to many other ocean island volcanoes where open-system processes such as magma mixing and significant partial melting of oceanic crust contribute to the formation of evolved magmas, and where there is less evidence for closed-system fractional crystallisation (Bohrson & Reid 1995, 1997; Caroff *et al.*, 1999; Carley *et al.*, 2011; Weismaier *et al.*, 2013; Longpré *et al.*, 2014; Sliwinski *et al.*, 2015). The main factor controlling whether open or closed system behaviour dominates could be the magmatic flux: it has been shown that increased magma fluxes correspond to increased degrees of crustal assimilation and crystal entrainment at mid-ocean ridges (Michael & Cornell, 1998). Ascension Island has an order of magnitude slower growth rate when compared with Hawaii (Sharp & Renne, 2005; Minshull *et al.*, 2010), and thus we infer a significantly lower magmatic flux, which led to the development of small-scale, short-lived magma storage regions, and closed-system evolution of felsic magmas. Multiple volcanic centres also display evidence for relatively closed-system evolution of mafic magmas by extensive fractional crystallisation to produce alkaline felsic magmas (e.g. Volcán Alcedo in the Galápagos [Geist *et al.*, 1995], Terceira, São Miguel and Graciosa in the Azores [Mungall & Martin, 1995; Larrea *et al.*, 2014; Jeffrey *et al.*, 2016], and the extinct Oki-Dōzen volcano, Japan [Brenna *et al.*, 2015]). These islands are all likely the result of low magma production rates, and are likely not related to deep-seated mantle hotspots (Hildenbrand *et al.*, 2014; Métrich *et al.*, 2014). Fractional crystallisation always requires the formation of a large volume of plutonic rocks as a by-product of extensive fractional crystallisation. Erupted lithic fragments or

surface exposures provide evidence for these plutonic rocks (Mungall & Martin, 1995; Larrea *et al.*, 2014; Brenna *et al.*, 2015; Jeffrey *et al.*, 2016).

Fractional crystallisation: the space problem

Extensive fractional crystallisation of $> 80\%$ mafic melt to produce the felsic magmas seen on small ocean islands such as Ascension Island and the Azores implies that significant volumes of plutonic material remain in the crust. While eruptive volumes are unconstrained at Ascension Island due to high erosion rates and dispersal over the ocean, the high degrees of fractionation responsible for the evolution of a single body of felsic magma suggest that significant volumes of plutonic rocks must exist in the crust. Taking the evolution from the NE Bay scoria to the Middleton's Ridge rhyolite as an example, in total the rhyolite represents only $\sim 9\%$ of the original mass of basalt. If we assume a modest eruptive volume of 0.2 km^3 (compared with the AD 1630 eruption from São Miguel which evacuated $\sim 0.85 \text{ km}^3$ of magma [DRE; Cole *et al.*, 1995]), then $\sim 2 \text{ km}^3$ of fractionated crystals, preserved as plutonic rocks, must remain in the crust. Erupted volumes and degree of fractionation vary between eruptions, yet as over 70 eruptions of felsic magma have occurred over the last 1 million years on Ascension (Preece *et al.*, 2016), then a minimum of $\sim 140 \text{ km}^3$ of plutonic rocks may remain in the crust, with no evidence for their rejuvenation preserved in any volcanic products on Ascension Island. This could be viewed as a minimum volume, given the lack of constraints on eruptive volumes, and the unknown number of magmatic (not necessarily eruptive) events. Evidence for a central nested plutonic core (Evangelidis *et al.*, 2004) and over-thickening of layer 3 (where magmatic evolution is interpreted to occur at Ascension Island, see above) has been observed in seismic reflection surveys (Klingelhöfer *et al.*, 2001). Evangelidis *et al.* (2004) suggest that the central high velocity region, inferred to consist of plutonic rocks (of unknown compositions), could have a volume approaching 7000

km³. This appears large compared to our minimum estimates (above), however small discrete bodies of plutonic rocks of varying composition would not be resolvable from the seismic reflection surveys, and therefore this volume represents an area affected by plutonism, not necessarily the volumes of individual plutonic bodies. Aside from over-thickening of layer 3 (Klingelhöfer *et al.*, 2001), it remains unclear how such large potential volumes of plutonic rocks are accommodated in thin oceanic crust, yet their presence seems vital for the formation of evolved melts in low magma flux ocean island volcanoes.

CONCLUSIONS

- There are no differences in whole-rock or crystal compositions between the lavas erupted in the same spatial regions of the island, suggesting that in the last 1 Myr the processes controlling mafic melt production and eruption have remained constant, even if the source region composition and degree of partial melting may have changed (cf. Jicha *et al.*, 2013).
- Spatial variation in crystallinity and in the composition and origin of crystals between mafic eruptive centres highlights heterogeneity in the lower crust under Ascension Island. The mafic magmas which erupted along the South Coast region, as well as the Green Mountain scoria sample from the felsic complex, incorporated higher volumes of antecrysts during magma ascent, consistent with the observation of increased numbers of coherent plutonic lithic fragments in these lava flows.
- Felsic melt evolution at Ascension Island is dominantly controlled by crystal fractionation of ternary feldspar, with minor fayalite or sodic clinopyroxene, dependent upon the ascent rate and oxidation state of the magma, with isotopic evidence of minor crustal assimilation of seawater-altered crustal material (Kar *et al.*, 1998). There is no evidence for magma mixing in any of the eruptive deposits studied

here, indicating that while a wide range of magma compositions are erupted across a ~12 km diameter island, they do not encounter other melts during their transport through the crust. Magmatic evolution occurs in small, short-lived, isolated magma storage regions in the lower crust. Antecrysts do not show reaction rims, and therefore their incorporation is purely mechanical and occurred late (during magma ascent).

- Alkali feldspar-melt hygrometry reveals high water concentrations of up to 8 wt % in the more-evolved magmas. These high H₂O concentrations, combined with the lack of evidence for an external trigger in the crystal chemistry, suggest that internal over-pressure from high degrees of fractional crystallisation concentrating H₂O in the liquid phase is a likely eruptive trigger for explosive eruptions on Ascension Island.
- Felsic magmas are almost entirely erupted in the central and eastern areas of Ascension Island, implying a spatial control on the evolution of felsic melts. We infer that the presence of significant volumes of plutonic bodies at depth inhibits magma ascent in these regions, and allows magmas to evolve and incorporate antecrysts. While the origin and nature of these plutonic bodies is not yet known, they must pre-date the subaerial stage of Ascension Island volcanism. The presence of plutonic rocks as abundant lithic clasts in the central and eastern regions highlights the importance of heterogeneous crustal structure in the evolution of magmas in the thin, young oceanic crust of Ascension Island.

ACKNOWLEDGEMENTS

In memory of the late Jon Davidson (1959–2016). We thank Marc Holland, the Ascension Island Government, the Heritage Society, the Conservation Department and island residents (in particular Drew Avery) for their logistical support during field seasons. George Cooper, Chris Hayward, Ian Schipper, Bertrand Lezé and Chris Ottley are thanked for their laboratory

and technical assistance during the course of analyses for this project. Vibrant discussions with Ben Cohen, Julia Crummy, Bridie Davies, Sue Loughlin, Darren Mark, Jane Scarrow, Fin Stuart, Charlotte Vye-Brown and Barry Weaver helped in formulating our ideas. Constructive and considered reviews by Marco Brenna, Felix Genske, Karen Harpp and an anonymous reviewer, and the expert editorial handling of Wendy Bohrsen have led to significant improvements to this manuscript.

FUNDING

This project was funded by a Leverhulme Trust Research Project Grant (RPG-2013-042), with the second field season supported by a Gloyne Outdoor Geological Research award from the Geological Society of London.

REFERENCES

- Ablay, G. J., Carroll, M. R., Palmer, M. R., Martí, J., & Sparks, R. S. J. (1998). Basanite–phonolite lineages of the Teide–Pico Viejo volcanic complex, Tenerife, Canary Islands. *Journal of Petrology*, 39(5), 905-936.
- Allan, A. S., Wilson, C. J., Millet, M. A., & Wysoczanski, R. J. (2012). The invisible hand: Tectonic triggering and modulation of a rhyolitic supereruption. *Geology*, 40(6), 563-566.
- Almeev, R., Holtz, F., Koepke, J., Haase, K., & Devey, C. (2008). Depths of partial crystallization of H₂O-bearing MORB: phase equilibria simulations of basalts at the MAR near Ascension Island (7–11 S). *Journal of Petrology*, 49(1), 25-45.
- Arth, J. G. (1976). Behavior of trace elements during magmatic processes: a summary of theoretical models and their applications. *J. Res. US Geol. Surv.:(United States)*, 4(1).
- Ashwal, L., Torsvik, T., Horváth, P., Harris, C., Webb, S., Werner, S., & Corfu, F. (2016). A

- Mantle-derived Origin for Mauritian Trachytes. *Journal of Petrology*, 57(9), 1645-1676
- Bacon, C. R. & Hirschmann, M. M. (1988). Mg/Mn partitioning as a test for equilibrium between coexisting Fe^{Ti} oxides. *American Mineralogist* 73, 57-61
- Bauer, K., Trumbull, R. B., & Vietor, T. (2003). Geophysical images and a crustal model of intrusive structures beneath the Messum ring complex, Namibia. *Earth and Planetary Science Letters*, 216(1-2), 65-80.
- Bohrson, W. A., & Reid, M. R. (1995). Petrogenesis of alkaline basalts from Socorro Island, Mexico: Trace element evidence for contamination of ocean island basalt in the shallow ocean crust. *Journal of Geophysical Research: Solid Earth*, 100(B12), 24555-24576.
- Bohrson, W. A., & Reid, M. R. (1997). Genesis of silicic peralkaline volcanic rocks in an ocean island setting by crustal melting and open-system processes: Socorro Island, Mexico. *Journal of Petrology*, 38(9), 1137-1166.
- Bohrson, W. A., Reid, M. R., Grunder, A. L., Heizler, M. T., Harrison, T. M., & Lee, J. (1996). Prolonged history of silicic peralkaline volcanism in the eastern Pacific Ocean. *Journal of Geophysical Research: Solid Earth*, 101(B5), 11457-11474.
- Bottinga, Y., & Weill, D. F. (1970). Densities of liquid silicate systems calculated from partial molar volumes of oxide components. *American Journal of Science*, 269(2), 169-182.
- Brenna, M., Nakada, S., Miura, D., Toshida, K., Ito, H., Hokanishi, N., & Nakai, S. I. (2015). A trachyte–syenite core within a basaltic nest: filtering of primitive injections by a multi-stage magma plumbing system (Oki-Dōzen, south-west Japan). *Contributions to Mineralogy and Petrology*, 170(2), 1-21.

- Burke, K. C., & Wilson, J. T. (1976). Hot spots on the Earth's surface. *Scientific American*, 235(2), 46-59.
- Caricchi, L., Sheldrake, T. E., & Blundy, J. (2018). Modulation of magmatic processes by CO₂ flushing. *Earth and Planetary Science Letters*, 491, 160-171.
- Carley, T. L., Miller, C. F., Wooden, J. L., Bindeman, I. N., & Barth, A. P. (2011). Zircon from historic eruptions in Iceland: reconstructing storage and evolution of silicic magmas. *Mineralogy and Petrology*, 102(1-4), 135-161.
- Caroff, M., Guillou, H., Lamiaux, M., Maury, R. C., Guille, G., & Cotten, J. (1999). Assimilation of ocean crust by hawaiitic and mugearitic magmas: an example from Eiao (Marquesas). *Lithos*, 46(2), 235-258.
- Carracedo, J.C., Badiola, E.R., Guillou, H., Paterne, M., Scaillet, S., Torrado, F.P., Paris, R., Fra-Paleo, U. & Hansen, A., (2007). Eruptive and structural history of Teide Volcano and rift zones of Tenerife, Canary Islands. *Geological Society of America Bulletin*, 119(9-10), 1027-1051.
- Chamberlain, K. J., Barclay, J., Preece, K., Brown, R. J., & Davidson, J. P. (2016). Origin and evolution of silicic magmas at ocean islands: Perspectives from a zoned fall deposit on Ascension Island, South Atlantic. *Journal of Volcanology and Geothermal Research*, 327, 349-360.
- Charlier, B. L. A., Wilson, C. J. N., Lowenstern, J. B., Blake, S., Van Calsteren, P. W., & Davidson, J. P. (2005). Magma generation at a large, hyperactive silicic volcano (Taupo, New Zealand) revealed by U–Th and U–Pb systematics in zircons. *Journal of Petrology*, 46(1), 3-32.
- Charlier, B., Namur, O., & Grove, T. L. (2013). Compositional and kinetic controls on liquid immiscibility in ferrobasalt–rhyolite volcanic and plutonic series. *Geochimica et Cosmochimica Acta*, 113, 79-93.

- Cole, P. D., Queiroz, G., Wallenstein, N., Gaspar, J. L., Duncan, A. M., & Guest, J. E. (1995). An historic subplinian/phreatomagmatic eruption: the 1630 AD eruption of Furnas volcano, São Miguel, Azores. *Journal of Volcanology and Geothermal Research*, 69(1), 117-135.
- Coogan, L.A., Kempton, P. D., Saunders, A. D., Norry, M. J. (2000): Melt aggregation within the crust beneath the Mid-Atlantic Ridge: evidence from plagioclase and clinopyroxene major and trace element compositions. *Earth and Planetary Science Letters*, 176(2), 245-257.
- Coombs, D. W. (1963). Trends and affinities of basaltic magmas and pyroxenes as illustrated on the diopside-olivine-silica diagram: in Miscellaneous papers—International Mineralogical Association Third General Meeting, Mineral. Soc. Amer., Spec. Pap., Vol. 1, p. 227-250.
- Daly, R. A. (1925, June). The geology of Ascension Island. In *Proceedings of the American Academy of Arts and Sciences* (Vol. 60, No. 1, pp. 3-80). American Academy of Arts & Sciences.
- Davidson J. P., Kar A. & Weaver B. L. (1997). The origin of extreme isotope signatures among differentiated rocks from Ascension Island. *Geological Society of America, Abstracts with Programs* 29, A-89.
- Davis, A. S., Clague, D. A., & Paduan, J. B. (2007). Diverse origins of xenoliths from seamounts at the continental margin, offshore central California. *Journal of Petrology*, 48(5), 829-852.
- Di Matteo, V., Carroll, M. R., Behrens, H., Vetere, F., & Brooker, R. A. (2004). Water solubility in trachytic melts. *Chemical Geology*, 213(1-3), 187-196.

- Druitt, T. H., Brenchley, P. J., Gökten, Y. E., & Francaviglia, V. (1995). Late Quaternary rhyolitic eruptions from the Acigöl Complex, central Turkey. *Journal of the Geological Society*, 152(4), 655-667.
- Eichelberger, J. C. (1995). Silicic volcanism: ascent of viscous magmas from crustal reservoirs. *Annual Review of Earth and Planetary Sciences*, 23(1), 41-63.
- Evangelidis, C. P., Minshull, T. A., & Henstock, T. J. (2004). Three-dimensional crustal structure of Ascension Island from active source seismic tomography. *Geophysical Journal International*, 159(1), 311-325.
- Ewart, A., & Griffin, W. L. (1994). Application of proton-microprobe data to trace-element partitioning in volcanic rocks. *Chemical Geology*, 117(1-4), 251-284.
- Fowler, S. J., & Spera, F. J. (2010). A metamodel for crustal magmatism: phase equilibria of giant ignimbrites. *Journal of Petrology*, 51(9), 1783-1830.
- Gazel, E., Hayes, J. L., Kelemen, P. B., Everson, E. D., Holbrook, W. S., & Vance, E. (2014, December). Generation of continental crust in intra-oceanic arcs. In *AGU Fall Meeting Abstracts* (Vol. 1, p. 4845).
- Geist, D. J., White, W. M., & McBirney, A. R. (1988). Plume-asthenosphere mixing beneath the Galapagos archipelago. *Nature*, 333(6174), 657.
- Geist, D., Howard, K. A., & Larson, P. (1995). The generation of oceanic rhyolites by crystal fractionation: the basalt-rhyolite association at Volcan Alcedo, Galapagos Archipelago. *Journal of Petrology*, 36(4), 965-982.
- Ghiorso, M. S., & Evans, B. W. (2008). Thermodynamics of rhombohedral oxide solid solutions and a revision of the Fe-Ti two-oxide geothermometer and oxygen-barometer. *American Journal of Science*, 308(9), 957-1039.

- Giordano, D., Romano, C., Dingwell, D. B., Poe, B., & Behrens, H. (2004). The combined effects of water and fluorine on the viscosity of silicic magmas. *Geochimica et Cosmochimica Acta*, 68(24), 5159-5168.
- Glazner, A. F. (2007). Thermal limitations on incorporation of wall rock into magma. *Geology*, 35(4), 319-322.
- Goldich, S. S., Ingamells, C. O., Suhr, N. H. & Anderson, D. H. (1967). Analyses of silicate rock and mineral standards. *Canadian Journal of Earth Sciences* 4, 747-755.
- Gualda, G. A., & Ghiorso, M. S. (2015). MELTS_Excel: A Microsoft Excel - based MELTS interface for research and teaching of magma properties and evolution. *Geochemistry, Geophysics, Geosystems*, 16(1), 315-324.
- Gualda, G. A., Ghiorso, M. S., Lemons, R. V., & Carley, T. L. (2012). Rhyolite-MELTS: a modified calibration of MELTS optimized for silica-rich, fluid-bearing magmatic systems. *Journal of Petrology*, 53(5), 875-890.
- Harpp, K. S., & White, W. M. (2001). Tracing a mantle plume: Isotopic and trace element variations of Galápagos seamounts. *Geochemistry, Geophysics, Geosystems*, 2(6).
- Harris, C. (1983). The petrology of lavas and associated plutonic inclusions of Ascension Island. *Journal of Petrology*, 24(4), 424-470.
- Harris, C. (1986). A quantitative study of magmatic inclusions in the plutonic ejecta of Ascension Island. *Journal of Petrology*, 27(1), 251-276.
- Harris, C., Bell, J. D., & Atkins, F. B. (1982). Isotopic composition of lead and strontium in lavas and coarse-grained blocks from Ascension Island, South Atlantic. *Earth and Planetary Science Letters*, 60(1), 79-85.
- Hildenbrand, A., Weis, D., Madureira, P., & Marques, F. O. (2014). Recent plate re-organization at the Azores Triple Junction: Evidence from combined geochemical and

- geochronological data on Faial, S. Jorge and Terceira volcanic islands. *Lithos*, 210, 27-39.
- Hobson, K.E. (2001). The pyroclastic deposits and eruption history of Ascension Island: a palaeomagnetic and volcanological study. *Doctoral dissertation, University of Oxford*.
- Humphreys, M. C., Christopher, T., & Hards, V. (2009). Microlite transfer by disaggregation of mafic inclusions following magma mixing at Soufrière Hills volcano, Montserrat. *Contributions to Mineralogy and Petrology*, 157(5), 609-624.
- Ingamells, C. O. (1980). Analysed minerals for electron microprobe standards. *Geostandards Newsletter* 2, 115.
- Jarosewich, E., Nelen, J. A. & Norberg, J. A. (1980). Reference samples for electron microprobe analysis. *Geostandards Newsletter* 4, 43-47.
- Jeffery, A. J., Gertisser, R., O'Driscoll, B., Pacheco, J. M., Whitley, S., Pimentel, A., & Self, S. (2016). Temporal evolution of a post-caldera, mildly peralkaline magmatic system: Furnas volcano, São Miguel, Azores. *Contributions to Mineralogy and Petrology*, 171(5), 1-24
- Jicha, B. R., Singer, B. S., & Valentine, M. J. (2013). $^{40}\text{Ar}/^{39}\text{Ar}$ Geochronology of Subaerial Ascension Island and a Re-evaluation of the Temporal Progression of Basaltic to Rhyolitic Volcanism. *Journal of Petrology*, 54(12), 2581-2596.
- Jochum, K. P., Weis, U., Stoll, B., Kuzmin, D., Yang, Q., Raczek, I., Jacob, D.E., Stracke, A., Birbaum, K., Frick, D.A. & Günther, D. (2011). Determination of reference values for NIST SRM 610–617 glasses following ISO guidelines. *Geostandards and Geoanalytical Research*, 35(4), 397-429.
- Jochum, K. P., Weis, U., Schwager, B., Stoll, B., Wilson, S. A., Haug, G. H., Andreae, M. O. & Enzweiler, J. (2016). Reference values following ISO guidelines for frequently

requested rock reference materials. *Geostandards and Geoanalytical Research*, 40(3), 333-350.

Kahl, M., Chakraborty, S., Costa, F., Pompilio, M., Liuzzo, M., & Viccaro, M. (2013).

Compositionally zoned crystals and real-time degassing data reveal changes in magma transfer dynamics during the 2006 summit eruptive episodes of Mt.

Etna. *Bulletin of Volcanology*, 75(2), 1-14

Kar, A. (1997). A comprehensive geological, geochemical, and petrogenetic study of hotspot-related oceanic basalt–rhyolite series rocks from Ascension Island, South Atlantic Ocean. Norman: University of Oklahoma. p. 260. Unpublished Ph.D. dissertation.

Kar, A., Weaver, B., Davidson, J., & Colucci, M. (1998). Origin of differentiated volcanic and plutonic rocks from Ascension Island, South Atlantic Ocean. *Journal of Petrology*, 39(5), 1009-1024.

Klingelhöfer, F., Minshull, T. A., Blackman, D. K., Harben, P., & Childers, V. (2001).

Crustal structure of Ascension Island from wide-angle seismic data: implications for the formation of near-ridge volcanic islands. *Earth and Planetary Science Letters*, 190(1), 41-56

Klügel, A. Hansteen, T. H. & Galipp, K. (2005). Magma storage and underplating beneath Cumbre Vieja volcano, La Palma (Canary Islands). *Earth and Planetary Science Letters* **236**, 211-226.

Koppers, A. A., & Staudigel, H. (2005). Asynchronous bends in Pacific seamount trails: a case for extensional volcanism? *Science*, 307(5711), 904-907.

Kuehn, S. C., Froese, D. G., Pearce, N. J., & Foit, F. F. (2009, December). ID3506, a new/old Lipari obsidian standard for characterization of natural glasses and for tephrochronology. In *AGU Fall Meeting Abstracts*.

- Kuritani, T., Yokoyama, T., Kitagawa, H., Kobayashi, K., & Nakamura, E. (2011). Geochemical evolution of historical lavas from Askja Volcano, Iceland: Implications for mechanisms and timescales of magmatic differentiation. *Geochimica et Cosmochimica Acta*, 75(2), 570-587.
- Larrea, P., Galé, C., Ubide, T., Widom, E., Lago, M., & França, Z. (2014). Magmatic Evolution of Graciosa (Azores, Portugal). *Journal of Petrology*, 55(11), 2125-2154.
- Lemarchand, F., Villemant, B., & Calas, G. (1987). Trace element distribution coefficients in alkaline series. *Geochimica et Cosmochimica Acta*, 51(5), 1071-1081.
- Longpré, M. A., Klügel, A., Diehl, A., & Stix, J. (2014). Mixing in mantle magma reservoirs prior to and during the 2011–2012 eruption at El Hierro, Canary Islands. *Geology*, 42(4), 315-318.
- Luhr, J. F., & Carmichael, I. S. (1990). Petrological monitoring of cyclical eruptive activity at Volcan Colima, Mexico. *Journal of Volcanology and Geothermal Research*, 42(3), 235-260.
- Mahood, G. A., & Stimac, J. A. (1990). Trace-element partitioning in pantellerites and trachytes. *Geochimica et Cosmochimica Acta*, 54(8), 2257-2276.
- Mahood, G., & Hildreth, W. (1983). Large partition coefficients for trace elements in high-silica rhyolites. *Geochimica et Cosmochimica Acta*, 47(1), 11-30.
- Mancini, A., Mattsson, H. B., & Bachmann, O. (2015). Origin of the compositional diversity in the basalt-to-dacite series erupted along the Heiðarsporður ridge, NE Iceland. *Journal of Volcanology and Geothermal Research*, 301, 116-127.
- Markl, G., Marks, M. A., & Frost, B. R. (2010). On the controls of oxygen fugacity in the generation and crystallization of peralkaline melts. *Journal of Petrology*, 51(9), 1831-1847.

- Meade, F. C., Troll, V. R., Ellam, R. M., Freda, C., Font, L., Donaldson, C. H., & Klonowska, I. (2014). Bimodal magmatism produced by progressively inhibited crustal assimilation. *Nature Communications*, 5, 4199.
- Métrich, N., Zanon, V., Créon, L., Hildenbrand, A., Moreira, M., & Marques, F. O. (2014). Is the ‘Azores hotspot’ a wet spot? Insights from the geochemistry of fluid and melt inclusions in olivine of Pico basalts. *Journal of Petrology*, 55(2), 377-393.
- Michael, P. J., & Cornell, W. C. (1998). Influence of spreading rate and magma supply on crystallization and assimilation beneath mid-ocean ridges: Evidence from chlorine and major element chemistry of mid-ocean ridge basalts. *Journal of Geophysical Research: Solid Earth*, 103(B8), 18325-18356.
- Minshull, T. A., Ishizuka, O., & Garcia-Castellanos, D. (2010). Long-term growth and subsidence of Ascension Island: Constraints on the rheology of young oceanic lithosphere. *Geophysical Research Letters*, 37(23).
- Mollo, S., Masotta, M., Forni, F., Bachmann, O., De Astis, G., Moore, G., & Scarlato, P. (2015). A K-feldspar–liquid hygrometer specific to alkaline differentiated magmas. *Chemical Geology*, 392, 1-8.
- Montelli, R., Nolet, G., Dahlen, F. A., Masters, G., Engdahl, E. R., & Hung, S. H. (2004). Finite-frequency tomography reveals a variety of plumes in the mantle. *Science*, 303(5656), 338-343.
- Montelli, R., Nolet, G., Dahlen, F. A., & Masters, G. (2006). A catalogue of deep mantle plumes: New results from finite - frequency tomography. *Geochemistry, Geophysics, Geosystems*, 7(11).
- Mungall, J. E., & Martin, R. F. (1995). Petrogenesis of basalt-comendite and basalt-pantellerite suites, Terceira, Azores, and some implications for the origin of ocean-island rhyolites. *Contributions to Mineralogy and Petrology*, 119(1), 43-55.

- Nash, W. P., & Crecraft, H. R. (1985). Partition coefficients for trace elements in silicic magmas. *Geochimica et Cosmochimica Acta*, 49(11), 2309-2322
- Niu, Y., Wilson, M., Humphreys, E. R., & O'hara, M. J. (2011). The origin of intra-plate ocean island basalts (OIB): the lid effect and its geodynamic implications. *Journal of Petrology*, 52(7-8), 1443-1468.
- Nielson, D. L., & Sibbett, B. S. (1996). Geology of Ascension Island, South Atlantic Ocean. *Geothermics*, 25(4), 427-448.
- Palme, H., & O'Neill, H. S. C. (2003). Cosmochemical estimates of mantle composition. *Treatise on Geochemistry*, 2, 568.
- Panjasawatwong, Y., Danyushevsky, L. V., Crawford, A. J., & Harris, K. L. (1995). An experimental study of the effects of melt composition on plagioclase-melt equilibria at 5 and 10 kbar: implications for the origin of magmatic high-An plagioclase. *Contributions to Mineralogy and Petrology*, 118(4), 420-432.
- Papale, P., Neri, A., & Macedonio, G. (1998). The role of magma composition and water content in explosive eruptions: 1. Conduit ascent dynamics. *Journal of Volcanology and Geothermal Research*, 87(1-4), 75-93.
- Paulick, H., Münker, C., & Schuth, S. (2010). The influence of small-scale mantle heterogeneities on Mid-Ocean Ridge volcanism: evidence from the southern Mid-Atlantic Ridge (7° 30' S to 11° 30' S) and Ascension Island. *Earth and Planetary Science Letters*, 296(3), 299-310.
- Pearce, J. A., & Norry, M. J. (1979). Petrogenetic implications of Ti, Zr, Y, and Nb variations in volcanic rocks. *Contributions to Mineralogy and Petrology*, 69(1), 33-47.
- Petrelli, M., Poli, G., Perugini, D., & Peccerillo, A. (2005). PetroGraph: A new software to visualize, model, and present geochemical data in igneous petrology. *Geochemistry, Geophysics, Geosystems*, 6(7).

- Preece, K., Mark, D. F., Barclay, J., Cohen, B. E., Chamberlain, K. J., Jowitt, C., Vye-Brown, C., Brown, R. J. (2018). Bridging the gap: $^{40}\text{Ar}/^{39}\text{Ar}$ dating of volcanic eruptions from the 'Age of Discovery'. *Geology*, 46(12), 1035-1038.
- Preece, K., Barclay, J., Brown, R., Mark, D. F., Chamberlain, K., Cohen, B. E., Vye-Brown, C. (2016) A 1 million year eruption history of Ascension Island: insights from stratigraphy and $^{40}\text{Ar}/^{39}\text{Ar}$ dating. *Cities on Volcanoes 9*, Puerto Varas, Chile, Nov, 2016
- Price, R. C., Gamble, J. A., Smith, I. E., Maas, R., Waight, T., Stewart, R. B., & Woodhead, J. (2012). The anatomy of an Andesite volcano: a time–stratigraphic study of andesite petrogenesis and crustal evolution at Ruapehu Volcano, New Zealand. *Journal of Petrology*, 53(10), 2139-2189.
- Putirka, K. D. (2008). Thermometers and barometers for volcanic systems. *Reviews in Mineralogy and Geochemistry*, 69(1), 61-120.
- Roedder, E., & Coombs, D. S. (1967). Immiscibility in Granitic Melts, Indicated by Fluid Inclusions in Ejected Granitic Blocks from Ascension Island. *Journal of Petrology*, 8(3), 417-451.
- Rooney, T. O., Hart, W. K., Hall, C. M., Ayalew, D., Ghiorso, M. S., Hidalgo, P., & Yirgu, G. (2012). Peralkaline magma evolution and the tephra record in the Ethiopian Rift. *Contributions to Mineralogy and Petrology*, 164(3), 407-426.
- Rollinson, H. R. (1993). *Using geochemical data: evaluation, presentation, interpretation*. Routledge.
- Scoates, J. S. (2000). The plagioclase–magma density paradox re-examined and the crystallization of Proterozoic anorthosites. *Journal of Petrology*, 41(5), 627-649.

- Sharp, W. D., & Renne, P. R. (2005). The $^{40}\text{Ar}/^{39}\text{Ar}$ dating of core recovered by the Hawaii Scientific Drilling Project (phase 2), Hilo, Hawaii. *Geochemistry, Geophysics, Geosystems*, 6(4).
- Sliwinski, J. T., Bachmann, O., Ellis, B. S., Dávila-Harris, P., Nelson, B. K., & Dufek, J. (2015). Eruption of Shallow Crystal Cumulates during Explosive Phonolitic Eruptions on Tenerife, Canary Islands. *Journal of Petrology*, 56(11), 2173-2194.
- Sparks, R. S. J., & Sigurdsson, H. (1987). The 1875 eruption of Askja volcano, Iceland: combined fractional crystallization and selective contamination in the generation of rhyolitic magma. *Mineralogical Magazine*, 51(360), 183-202.
- Stock, M. J., Humphreys, M. C., Smith, V. C., Isaia, R., & Pyle, D. M. (2016). Late-stage volatile saturation as a potential trigger for explosive volcanic eruptions. *Nature Geoscience*, 9(3), 249.
- Stormer, J. C., & Nicholls, J. (1978). XLFRAC: a program for the interactive testing of magmatic differentiation models. *Computers & Geosciences*, 4(2), 143-159.
- Sverrisdottir, G. (2007). Hybrid magma generation preceding Plinian silicic eruptions at Hekla, Iceland: evidence from mineralogy and chemistry of two zoned deposits. *Geological Magazine*, 144(04), 643-659.
- Troll, V. R., & Schmincke, H. U. (2002). Magma mixing and crustal recycling recorded in ternary feldspar from compositionally zoned peralkaline ignimbrite 'A', Gran Canaria, Canary Islands. *Journal of Petrology*, 43(2), 243-270.
- Watson, E. B., & Green, T. H. (1981). Apatite/liquid partition coefficients for the rare earth elements and strontium. *Earth and Planetary Science Letters*, 56, 405-421.
- Weaver, B. L., Wood, D. A., Tarney, J., & Joron, J. L. (1987). Geochemistry of ocean island basalts from the south Atlantic: Ascension, Bouvet, St. Helena, Gough and Tristan da Cunha. *Geological Society, London, Special Publications*, 30(1), 253-267.

- Weaver, B., Kar, A., Davidson, J., & Colucci, M. (1996). Geochemical characteristics of volcanic rocks from Ascension Island, South Atlantic Ocean. *Geothermics*, 25(4), 449-470.
- Webster, J. D., & Rebbert, C. R. (2001). The geochemical signature of fluid-saturated magma determined from silicate melt inclusions in Ascension Island granite xenoliths. *Geochimica et Cosmochimica Acta*, 65(1), 123-136.
- Weis, D., Demaiffe, D., Cauet, S., & Javoy, M. (1987). Sr, Nd, O and H isotopic ratios in Ascension Island lavas and plutonic inclusions; cogenetic origin. *Earth and Planetary Science Letters*, 82(3), 255-268.
- Wiesmaier, S., Troll, V. R., Wolff, J. A., & Carracedo, J. C. (2013). Open-system processes in the differentiation of mafic magma in the Teide–Pico Viejo succession, Tenerife. *Journal of the Geological Society*, 170(3), 557-570.
- White, J. C., Holt, G. S., Parker, D. F., & Ren, M. (2003). Trace-element partitioning between alkali feldspar and peralkalic quartz trachyte to rhyolite magma. Part I: Systematics of trace-element partitioning. *American Mineralogist*, 88(2-3), 316-329.
- White, J. C., Parker, D. F., & Ren, M. (2009). The origin of trachyte and pantellerite from Pantelleria, Italy: insights from major element, trace element, and thermodynamic modelling. *Journal of Volcanology and Geothermal Research*, 179(1), 33-55.
- Zhao, D. (2004). Global tomographic images of mantle plumes and subducting slabs: insight into deep Earth dynamics. *Physics of the Earth and Planetary Interiors*, 146(1), 3-34.

FIGURE CAPTIONS

Figure 1: Geological map of Ascension Island, located 90 km from the Mid-Atlantic Ridge, between the Ascension Fracture Zone (AFZ) and the Boca Verde Fracture Zone (BVFZ; inset), adapted from Weaver *et al.* (1995), Paulick *et al.* (2010) and Chamberlain *et al.* (2016). Sample locations indicated by triangles, diamonds and pentagons; eruptive centres identified in grey font. Surface expressions of known faults outlined in red. Major lava flow boundaries are indicated with black lines in the mafic lava flows.

Figure 2: (a) Radiogenic isotope variations in Ascension Island lavas (subaerial unless otherwise stated); (b) Trace HFSE variation with major element variations; (c) Adapted from Jicha *et al.*, 2013, trace element variation in Ascension lavas, showing the variation due to source heterogeneity, differentiation, and Fe-Ti oxide controlled fractionation paths; (d) Variation in $^{143}\text{Nd}/^{144}\text{Nd}$ with degree of evolution (MgO). All data presented are a combination of Weaver *et al.* (1995, grey diamonds), Kar *et al.* (1998, orange diamonds), Paulick *et al.* (2010, blue squares) and Jicha *et al.* (2013, crosses).

Figure 3: (a) Whole-rock compositions of selected samples compared with all known Ascension Island whole-rock data shown as a grey field (data from Weaver *et al.*, 1996; Kar *et al.*, 1998; Jicha *et al.*, 2013). Diagram adapted from LeMaitre *et al.* (1989). (b) Primitive mantle (Palme & O'Neill, 2003) normalised trace element ranges for mafic-intermediate lavas (purple), scoria samples (orange), pumice samples (yellow) and felsic lava samples (blue).

Figure 4: Whole-rock variation in major and trace elements for all studied samples of Ascension Island mafic-intermediate lavas (purple triangles), felsic lavas (blue pentagons) and pyroclastics both pumiceous (yellow diamonds) and scoriaceous

(orange diamonds). Grey fields represent the full range of compositions found at Ascension from Weaver *et al.* (1995). For full data set, see Supplementary Data Appendix 2.

Figure 5: Photomicrographs of Ascension lava samples. (a,b): Young South Coast lava sample showing a glomerocryst of feldspar and olivine; (c,d): Young Sisters lava sample showing euhedral plagioclase feldspar in a microcrystalline matrix; (e,f): Cricket Valley lava with sodic feldspars and minor aegirine-augite in a microcrystalline groundmass; (g): Letterbox felsic lava with large ternary feldspar phenocrysts in a microcrystalline groundmass; (h): Ariane lava flow with ternary feldspars and aegirine-augite in a microcrystalline groundmass. Images (a, c, e, g) in plane-polarised light; images (b, d, f, h) in cross-polarised light. Sample numbers relate to those listed in Table 1 and numbers in square brackets show whole-rock SiO₂ concentrations.

Figure 6: Back Scattered Electron (BSE) images of Ascension Island lavas. Sample numbers relate to those listed in Table 1 and numbers in square brackets show whole-rock SiO₂ concentrations. Features labelled in red refer to A: Reverse-zoned feldspar; B: Normally-zoned olivine; C: Faint oscillatory-zoned plagioclase. D: Mafic lava groundmass, typically consisting of feldspar + olivine + magnetite ± clinopyroxene ± ilmenite; E: Unzoned feldspar typical of felsic products; F: Unzoned fayalitic olivine; G: Groundmass of felsic lavas flows consists dominantly of feldspar with minor interstitial aegirine and fayalite; H: Dark in BSE, cristobalite with characteristic fish-scale textures replacing groundmass and some feldspar crystals.

Figure 7: Ternary feldspar diagrams showing all feldspars differentiated by composition and eruptive style. For full data set see Supplementary Data Appendix 2.

Figure 8: Compositions of feldspars from (a) mafic to intermediate lavas; (b) felsic lavas and (c, d) all Ascension Island samples. Sample areas relate to those in Table 1. For full

data set see Supplementary Data Appendix 2. The purple field in (b) shows the compositions of feldspars from mafic to intermediate lava samples. The pink field in (b) shows Mid-Atlantic Ridge ocean crust feldspars from the Kane Fracture Zone (Coogan *et al.*, 2000). Core-rim differences within individual samples shown by filled (core) and open (rim) symbols in (c); sample colours and shapes refer to those listed in the key on (c).

Figure 9: Variation in plagioclase (a) and olivine (b) compositions with whole-rock SiO₂ (a) or Mg# (b), and the calculated equilibrium compositions of the respective crystal phases based on whole-rock XRF data (Table 1, and Supplementary Data Appendix 2). In (a) equilibrium compositions of feldspar are calculated at 1150 °C and 330 MPa (black) and 1050 °C and 330 MPa (grey) respectively, based on feldspar-melt and Fe-Ti oxide thermometry (see Table 8), and the pressure at the base of the crust at Ascension Island (Klingelhöfer, 2001).

Figure 10: Compositions of olivines from (a) mafic to intermediate lavas; (b) all pyroclastic samples. Variations between core and rim compositions shown in (c), where open symbols refer to rim analyses, and filled symbols core analyses. Sample areas relate to those in Table 1. For full data set see Supplementary Data Appendix 2. The purple field in (b) shows the compositions of olivines from mafic to intermediate lava samples.

Figure 11: Compositions of pyroxenes from all Ascension Island samples. Triangles refer to mafic to intermediate lava samples; squares and circles are felsic lava samples. Sample areas relate to those in Table 1. For full data set see Supplementary Data Appendix 2.

Figure 12: Matrix glass compositions from all Ascension Island samples. Sample areas relate to those in Table 1. For full data set see Supplementary Data Appendix 2.

Figure 13: Combined liquid lines of descent modelled from AI14-438 (to 950 °C, end marked by dashed line) and AI-621 (< 950 °C, start from dashed line) using rhyolite-MELTS

(Gualda & Ghiorso, 2015) at 330 MPa, 250 MPa, 170 MPa and 90 MPa. Purple ticks mark 20% increments of melt fraction remaining; grey ticks mark 10% melt fraction remaining, black ticks show liquid composition at 5% melt fraction remaining. Initial water concentrations for AI-438 were 0.5 wt % H₂O, based on MAR glasses showing a component of the fertile mantle end-member suggested to be the source of magmatism at Ascension Island (Almeev *et al.*, 2008; Paulick *et al.*, 2010). XRF data used are a combination of data presented here and in Weaver *et al.* (1996) and Kar (1997).

Figure 14: Modelled fractionating crystal compositions from MELTS (purple symbols representing different pressures of crystallisation, Gualda & Ghiorso, 2015) compared with those measured in this study (grey symbols). The decompression trend (black crosses) represents isothermal decompression at 800 °C from 90 to 1 MPa.

Figure 15: Trace element fractional crystallisation modelling following the four stages using Petrograph (Petrelli *et al.*, 2005). XRF data used for the modelling shown in diamonds, the resultant modelled liquid as diamonds. Each stage (1 – 4, connected by dashed lines) represents 0.92, 0.40, 0.16 and 0.07 total melt fraction remaining. Total XRF data field in grey is a combination of data presented here, and in Weaver *et al.*, 1996 and Kar, 1997. For the 4 stages and full modelled compositions and references for partition coefficients used, see Supplementary Data Appendix 3. The dashed field in (a) represents a subset of samples which plot towards syenitic samples from Ascension (not sampled in this study) and thus not modelled here.

Figure 16: Magmatic plumbing system model for Ascension Island - magma storage regions are not to scale. Note the geographic variation in the distribution of plutonic bodies (mafic plutonic rocks in blue, zone of nested felsic plutonic rocks hashed, with examples in purple) within the crust. Magma ascent paths shown in red (mafic) and purple-blue (felsic). Crustal structure from Klingelhöfer *et al.* (2001).

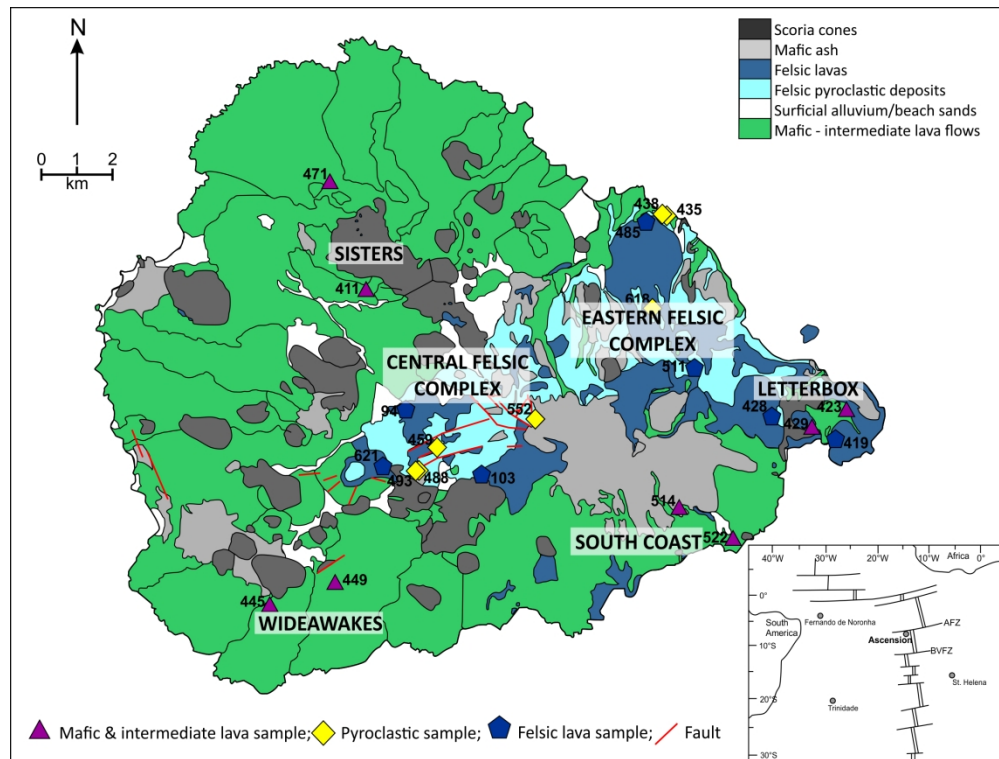


Figure 1: Geological map of Ascension Island, located 90 km from the Mid Atlantic Ridge and between the Ascension Fracture Zone (AFZ) and Boca Verde Fracture Zone (BVZF; inset), adapted from Weaver et al. (1995), Paulick et al. (2010) & Chamberlain et al. (2016). Sample locations indicated by triangles, diamonds and pentagons; eruptive centres identified in grey font. Surface expressions of known faults outlined in red. Major lava flow boundaries are indicated with black lines in the mafic lava flows.

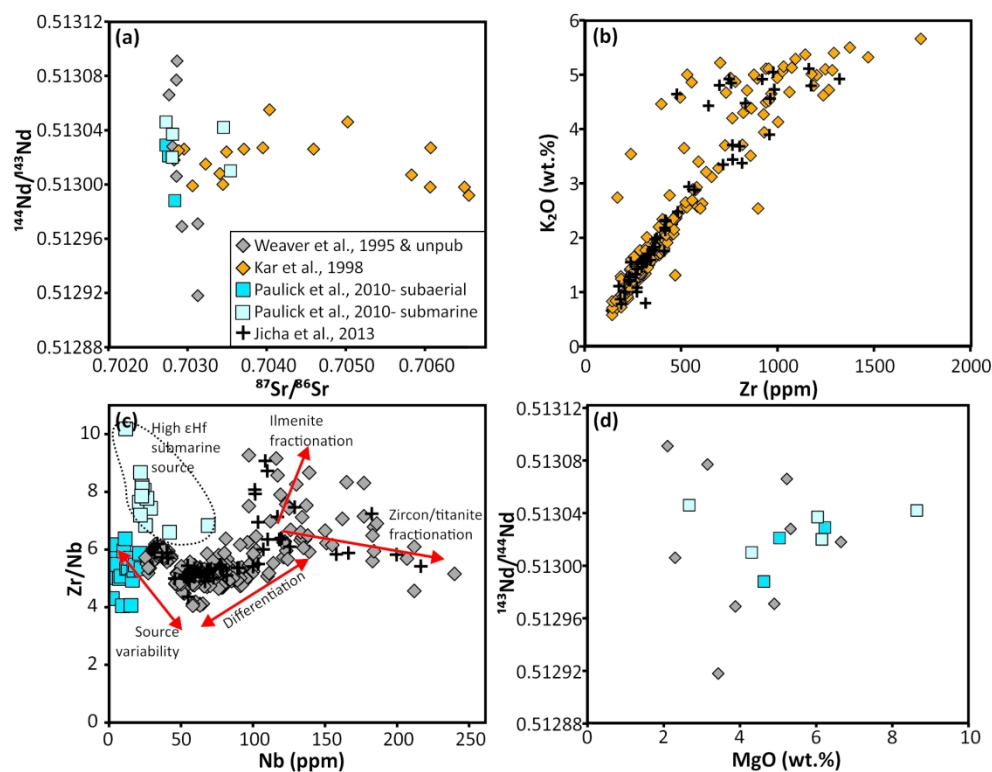


Figure 2: (a) Radiogenic isotope variations in Ascension Island lavas (subaerial unless otherwise stated); (b) Trace HFSE variation with major element variations; (c) Adapted from Jicha et al., 2013, trace element variation in Ascension lavas, showing the variation due to source heterogeneity, differentiation, and Fe-Ti oxide controlled fractionation paths; (d) variation in $^{143}\text{Nd}/^{144}\text{Nd}$ with degree of evolution (MgO). All data presented is a combination of Weaver et al. (1995, grey diamonds), Kar et al. (1998, orange diamonds), Paulick et al. (2010, blue squares) and Jicha et al. (2013, crosses).

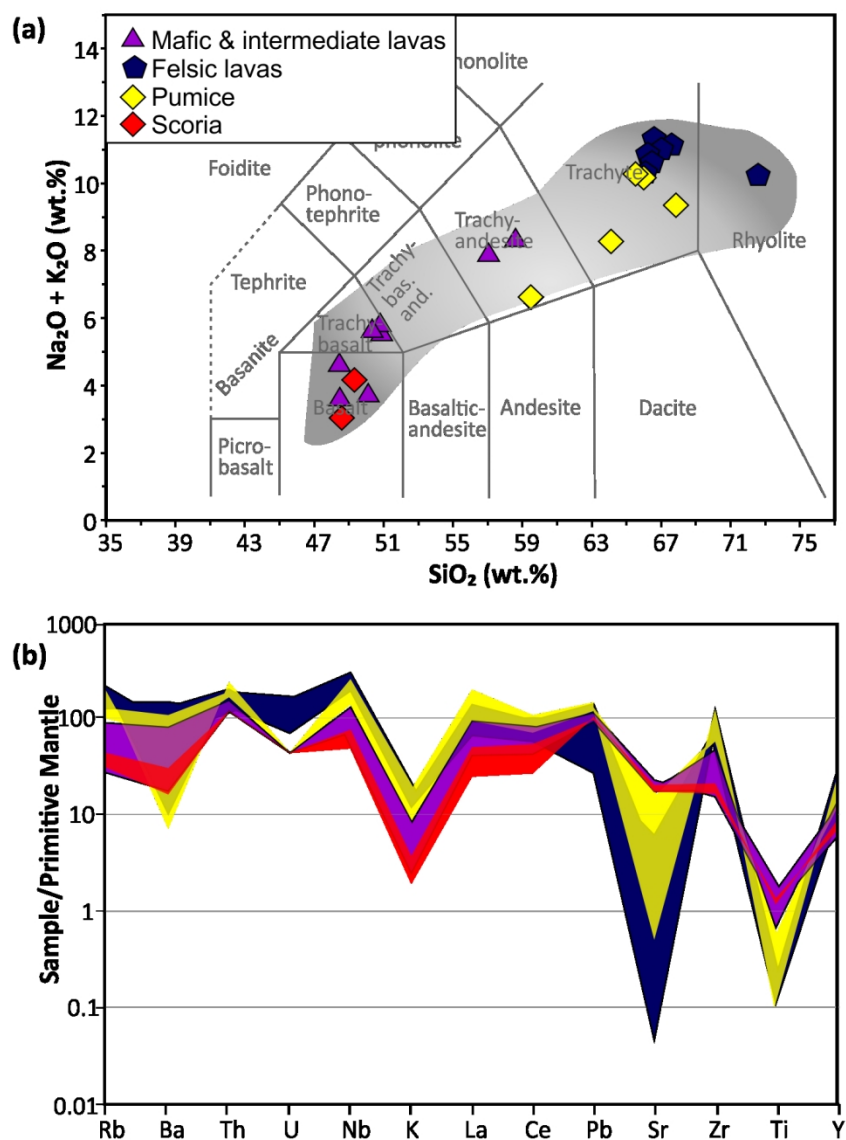


Figure 3: (a) Whole rock compositions of selected samples compared with all known Ascension Island whole rock data in grey field- (data from Weaver et al., 1996, Kar et al., 1998, Jicha et al., 2013). Diagram adapted from LeMaitre et al. (1989). (b) Primitive mantle (Palme & O'Neill, 2003) normalised trace element ranges for mafic-intermediate lavas (purple), scoria samples (orange), pumice samples (yellow) and felsic lava samples (blue).

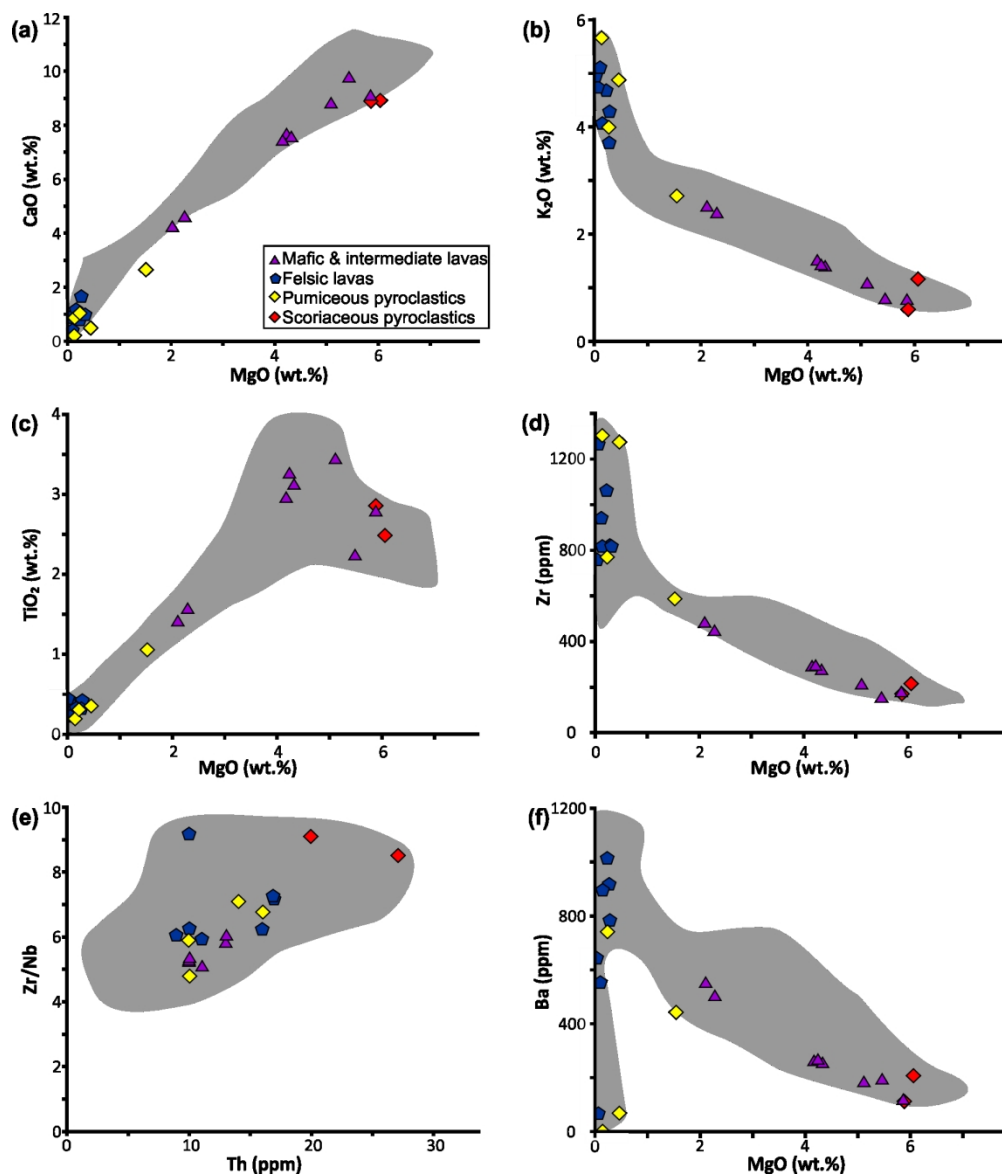


Figure 4: Whole rock variation in major and trace elements for all studied samples of Ascension Island mafic-intermediate lavas (purple triangles), felsic lavas (blue pentagons) and pyroclastics both pumiceous (yellow diamonds) and scoriaceous (orange diamonds). Grey fields represent the full range of compositions found at Ascension from Weaver et al. (1995). For full data set, see Electronic Appendix 2.

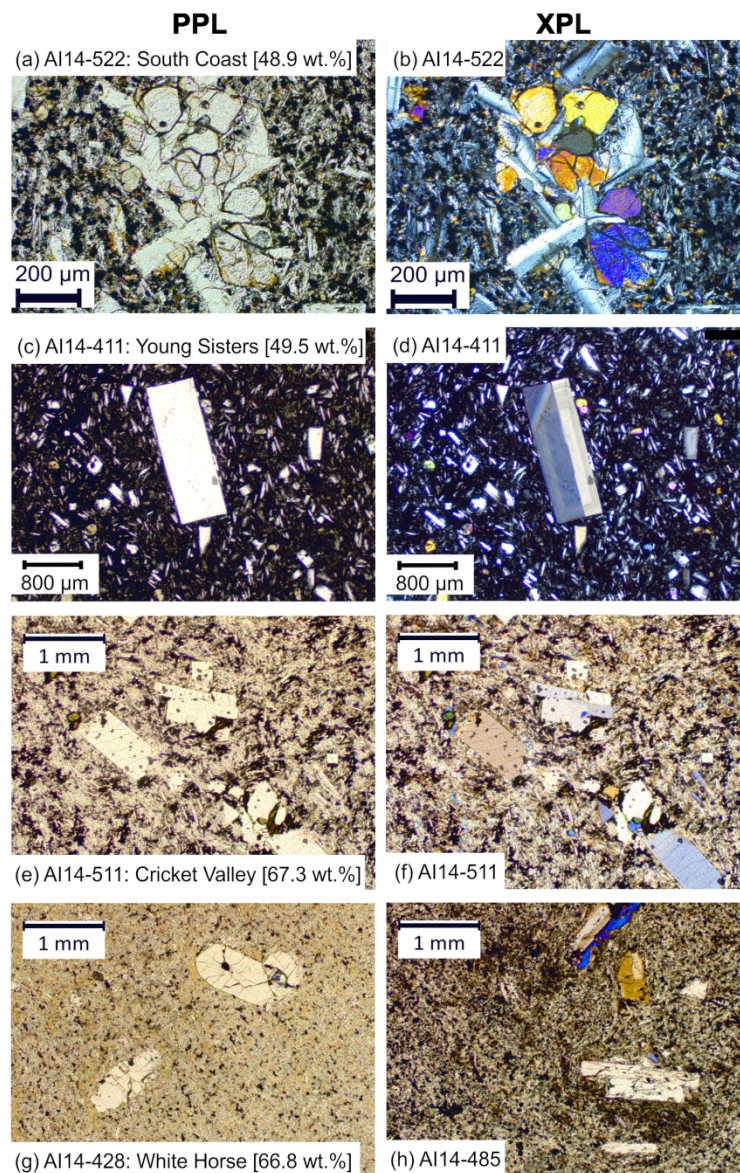


Figure 5: Photomicrographs of Ascension lava samples. (a, b): Young South Coast lava sample showing a glomerocryst of feldspar and olivine; (c, d): Young Sisters lava sample showing euhedral plagioclase feldspar in a microcrystalline matrix; (e, f): Cricket Valley lava with sodic feldspars and minor aegirine-augite in a microcrystalline groundmass; (g): Letterbox felsic lava with large ternary feldspar phenocrysts in a microcrystalline groundmass; (h): Ariane lava flow with ternary feldspars and aegirine-augite in a microcrystalline groundmass. Images (a, c, e, g) in plane-polarised light; images (b, d, f, h) in cross-polarised light. Sample numbers relate to those listed in Table 1 and numbers in square brackets show whole rock SiO₂ concentrations.

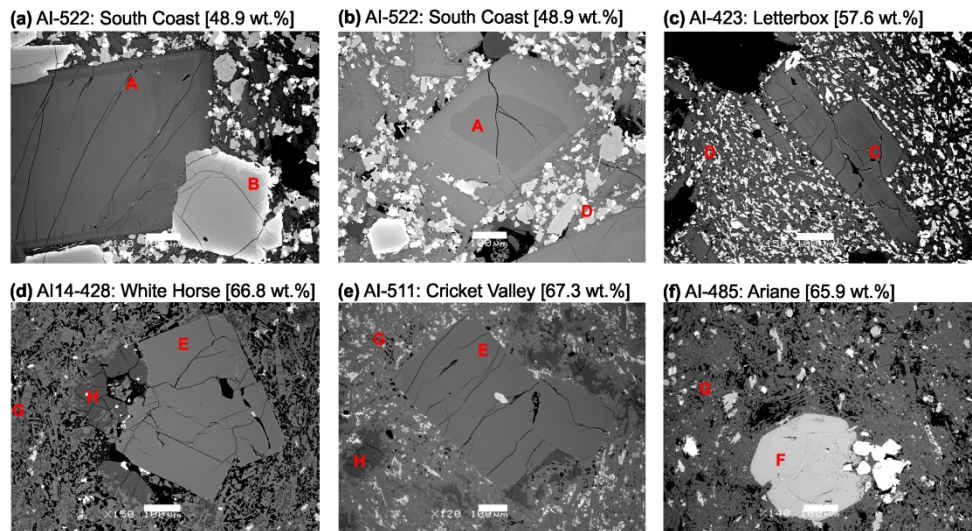


Figure 6: Back Scattered Electron (BSE) images of Ascension Island lavas. Sample numbers relate to those listed in Table 1 and numbers in square brackets show whole rock SiO₂ concentrations. Features labelled in red refer to A: Reverse-zoned feldspar; B: Normally-zoned olivine; C: Faint oscillatory-zoned plagioclase. D: Mafic lava groundmass, typically consisting of feldspar + olivine + magnetite ± clinopyroxene ± ilmenite; E: Unzoned feldspar typical of felsic products; F: Unzoned fayalitic olivine; G: Groundmass of felsic lavas flows consists dominantly of feldspar with minor interstitial aegirine and fayalite; H: Dark in BSE cristobalite with characteristic fish-scale textures replacing groundmass and some feldspar crystals.

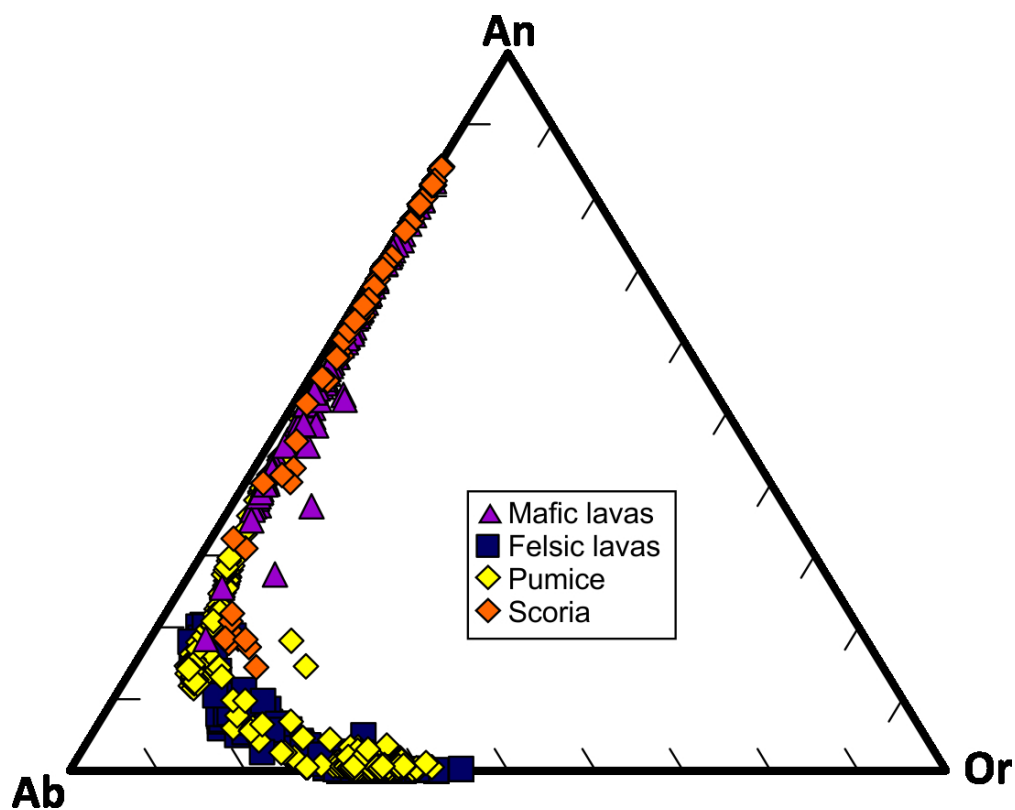


Figure 7: Ternary feldspar diagrams showing all feldspars differentiated by composition and eruptive style.
For full data set see Electronic Appendix 2.

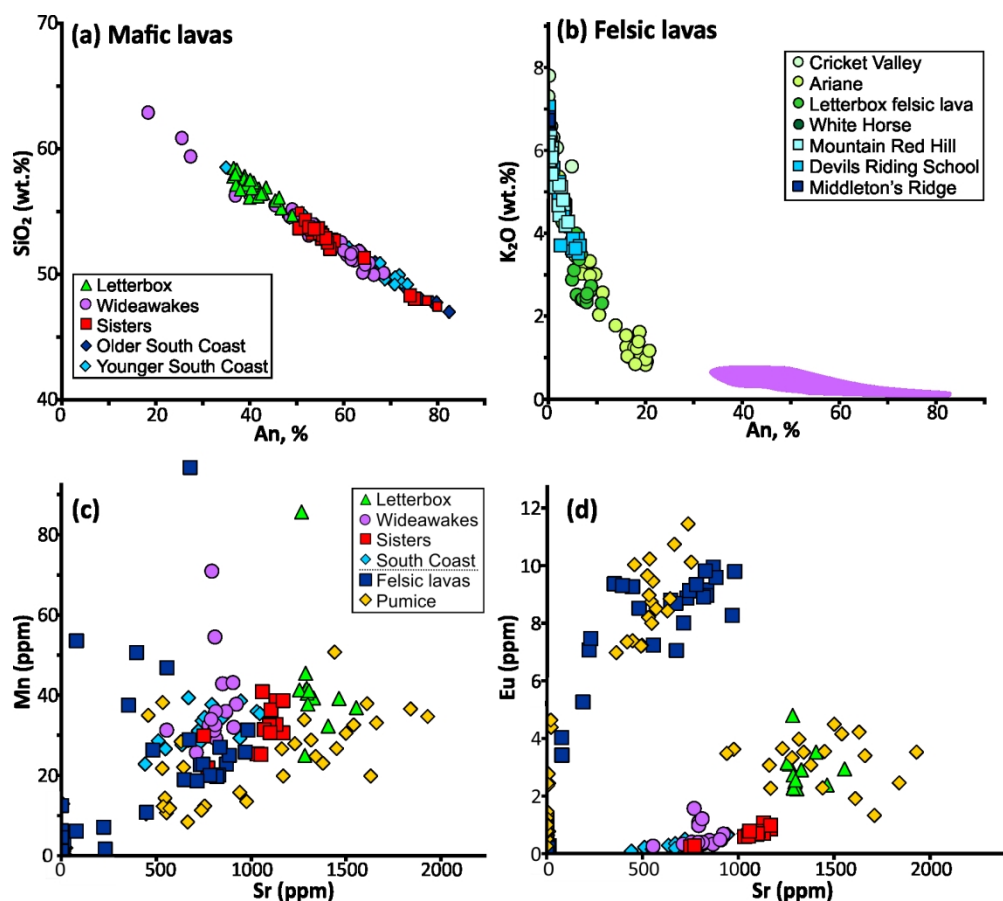


Figure 8: Compositions of feldspars from (a) mafic to intermediate lavas; (b) felsic lavas and (c, d) all Ascension Island samples. Sample areas relate to those used in Table 1. For full data set see Electronic Appendix 2. The purple field on panel (b) shows the compositions of feldspars from mafic to intermediate lava samples. The pink field on panel (b) shows the Mid Atlantic Ridge ocean crust feldspars from the Kane Fracture Zone (Coogan et al., 2000). Core-rim differences within individual samples shown by filled (core) and open (rim) symbols in (c); sample colours and shapes refer to those listed in the key on (c).

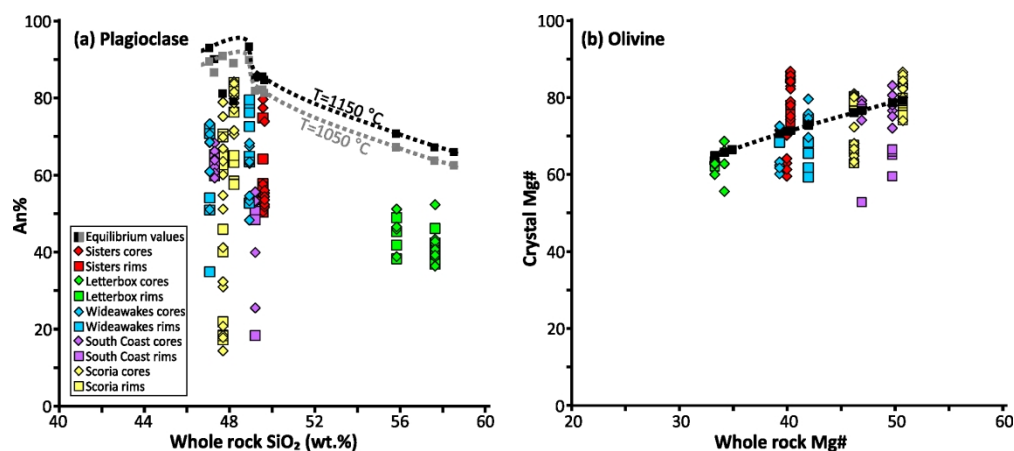


Figure 9: Variation in plagioclase (a) and olivine (b) compositions with whole rock SiO₂ (a) or Mg# (b), and the calculated equilibrium compositions of the respective crystal phases based on whole rock XRF data (Table 1, and Electronic Appendix 2). In (a) equilibrium compositions of feldspar are calculated at 1150 °C and 330 MPa (black) and 1050 °C and 330 MPa (grey) respectively, based on feldspar-melt and Fe-Ti oxide thermometry (see Table 8), and the pressure at the base of the crust at Ascension Island (Klingelhöfer, 2001).

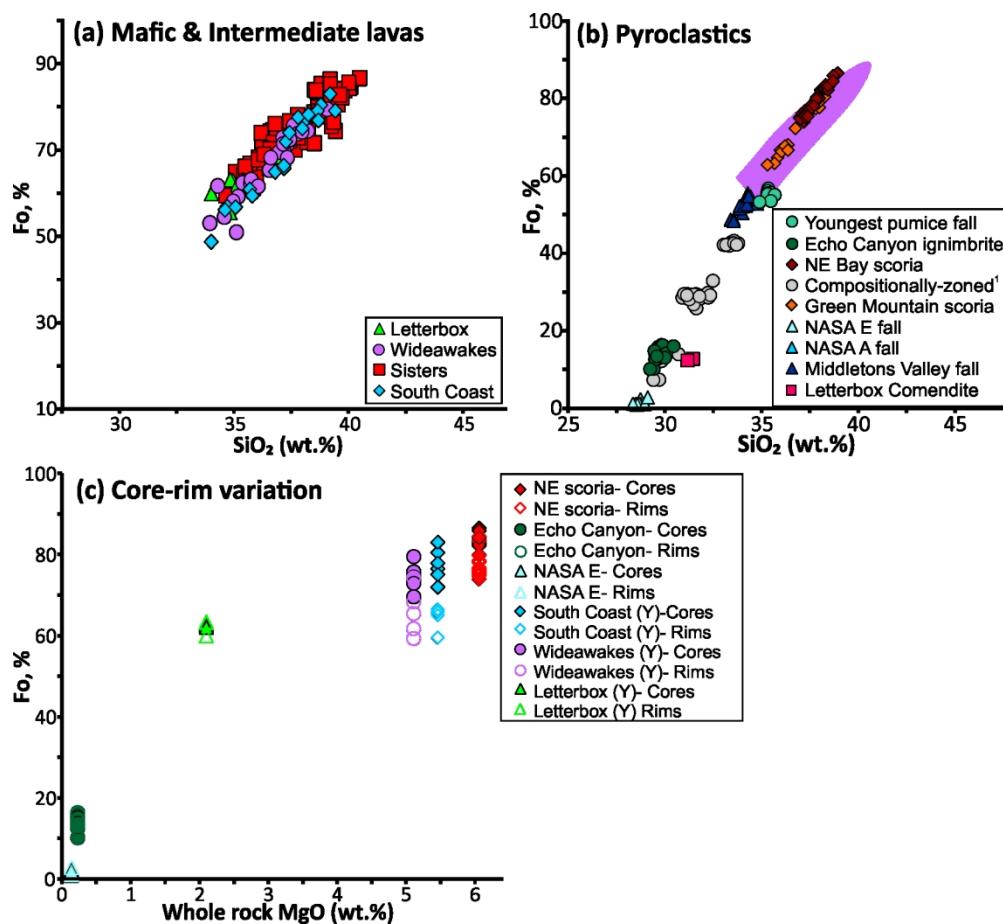


Figure 10: Compositions of olivines from (a) mafic to intermediate lavas; (b) all pyroclastic samples. Variations between core and rim compositions shown in panel (c), where open symbols refer to rim analyses, and filled symbols core analyses. Sample areas relate to those used in Table 1. For full data set see Electronic Appendix 2. The purple field on (b) shows the compositions of olivines from mafic to intermediate lava samples.

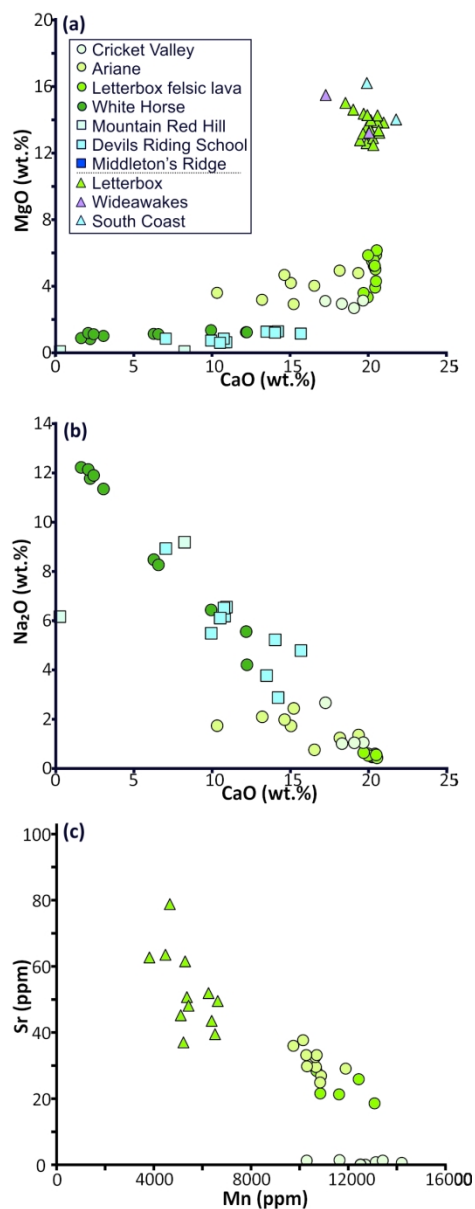


Figure 11: Compositions of pyroxenes from all Ascension Island samples. Triangles refer to samples of mafic to intermediate lava samples; squares and circles are felsic lava samples. Sample areas relate to those used in Table 1. For full data set see Electronic Appendix 2.

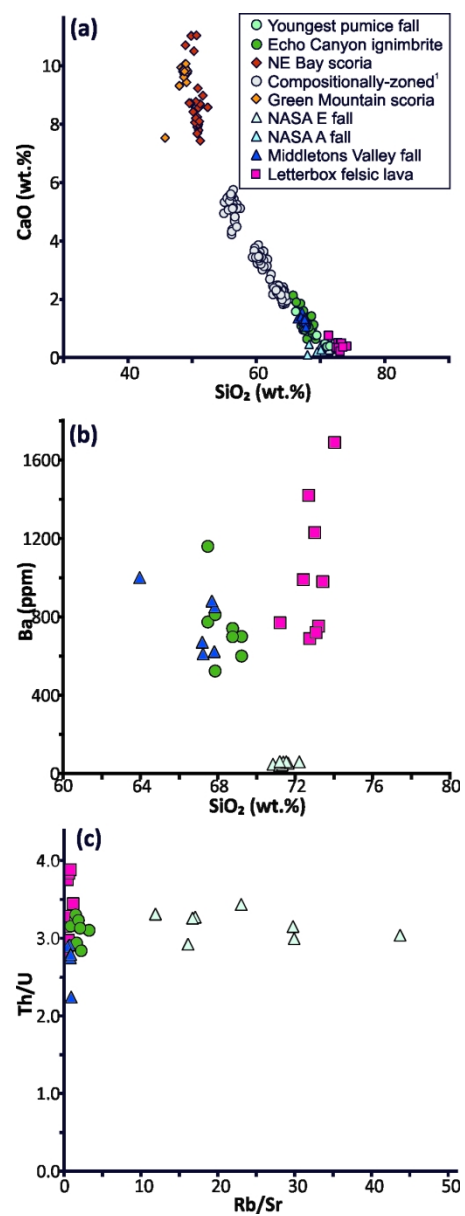


Figure 12: Matrix glass compositions from all Ascension Island samples. Sample areas relate to those used in Table 1. For full data set see Electronic Appendix 2.

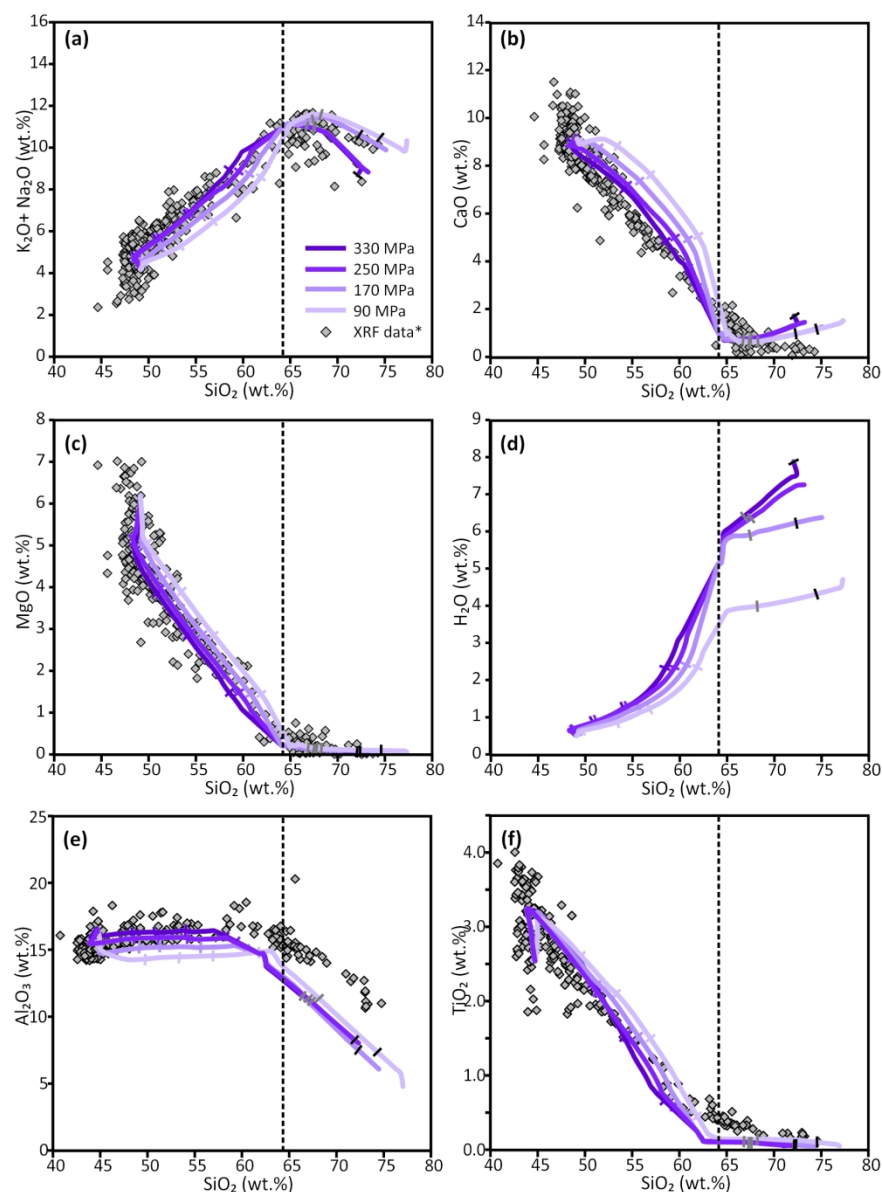


Figure 13: Combined liquid lines of descent modelled from AI14-438 (to 950 °C, end marked by dashed line) and AI-621 (< 950 °C, start from dashed line) using rhyolite-MELTS (Gualda & Ghiorso, 2015) at 330 MPa, 250 MPa, 170 MPa and 90 MPa. Purple ticks mark 20% increments of melt fraction remaining; grey ticks mark 10% melt fraction remaining, black ticks show liquid composition at 5% melt fraction remaining. Initial water concentrations for AI-438 were 0.5 wt.% H_2O , from MAR glasses showing a component of the fertile mantle end member suggested to be the source of magmatism at Ascension Island (Almeev et al., 2008; Paulick et al., 2010). *XRF data used is a combination of data presented here and Weaver et al. (1996) and Kar (1997).

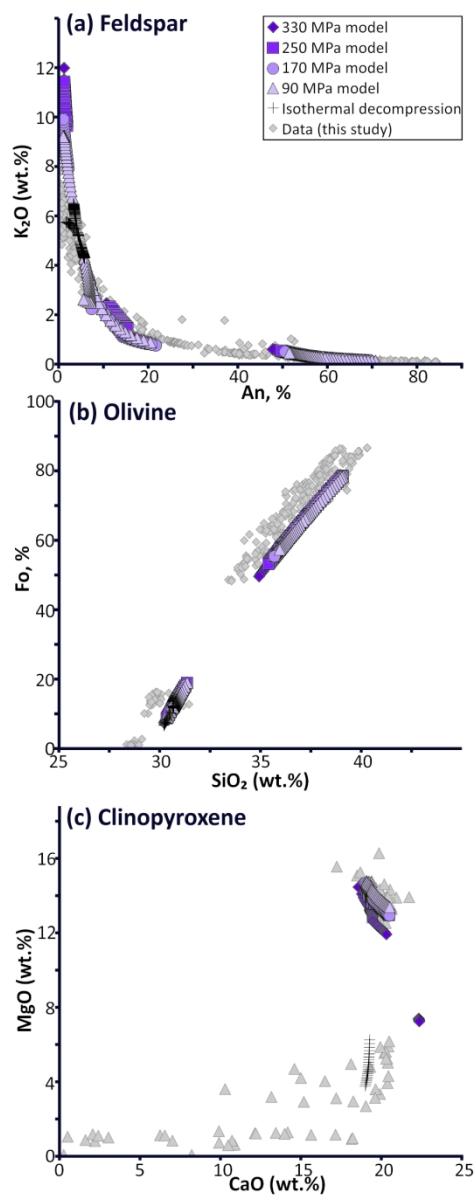


Figure 14: Modelled fractionating crystal compositions from MELTS (purple symbols representing different pressures of crystallisation, Gualda & Ghiorso, 2015) compared with those measured in this study (grey symbols). The decompression trend (black crosses) represents isothermal decompression at 800 °C from 90 to 1 MPa.

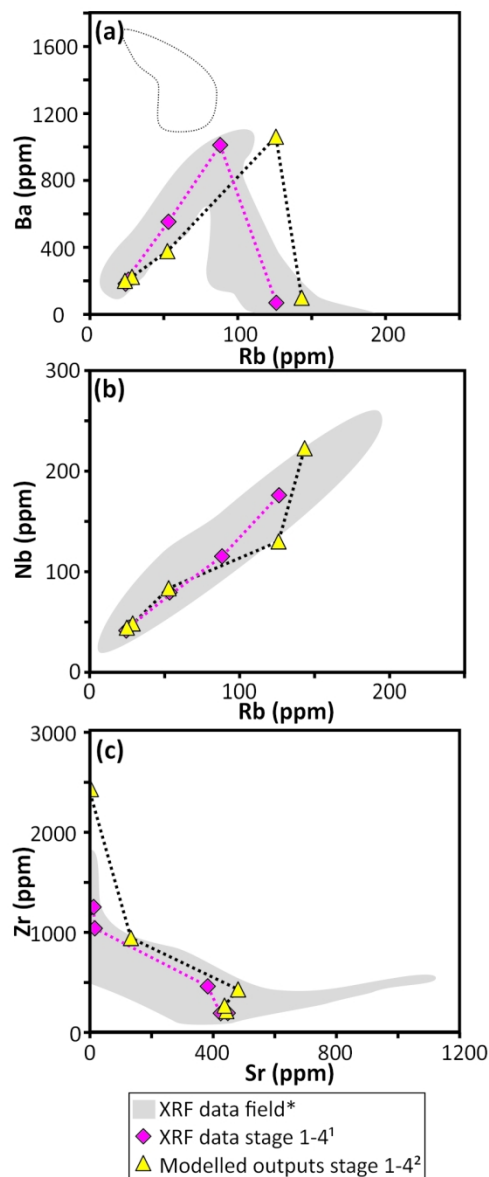


Figure 15: Trace element fractional crystallisation modelling following the stages modelling using Petrograph (Petrelli et al., 2005). XRF data used for the modelling shown in diamonds, the resultant modelled liquid as diamonds. Each stage (1 – 4, connected by dashed lines) represents 0.92, 0.40, 0.16, 0.07 total melt fraction remaining. *Total XRF data field in grey is a combination of data presented here, and Weaver et al., 1996 and Kar, 1997. 1, 2: For stages and full modelled compositions and references for partition coefficients used, see Electronic Appendix 3. The dashed field in (a) represents a subset of samples which plot towards syenitic samples of Ascension (not sampled in this study) and thus not modelled here.

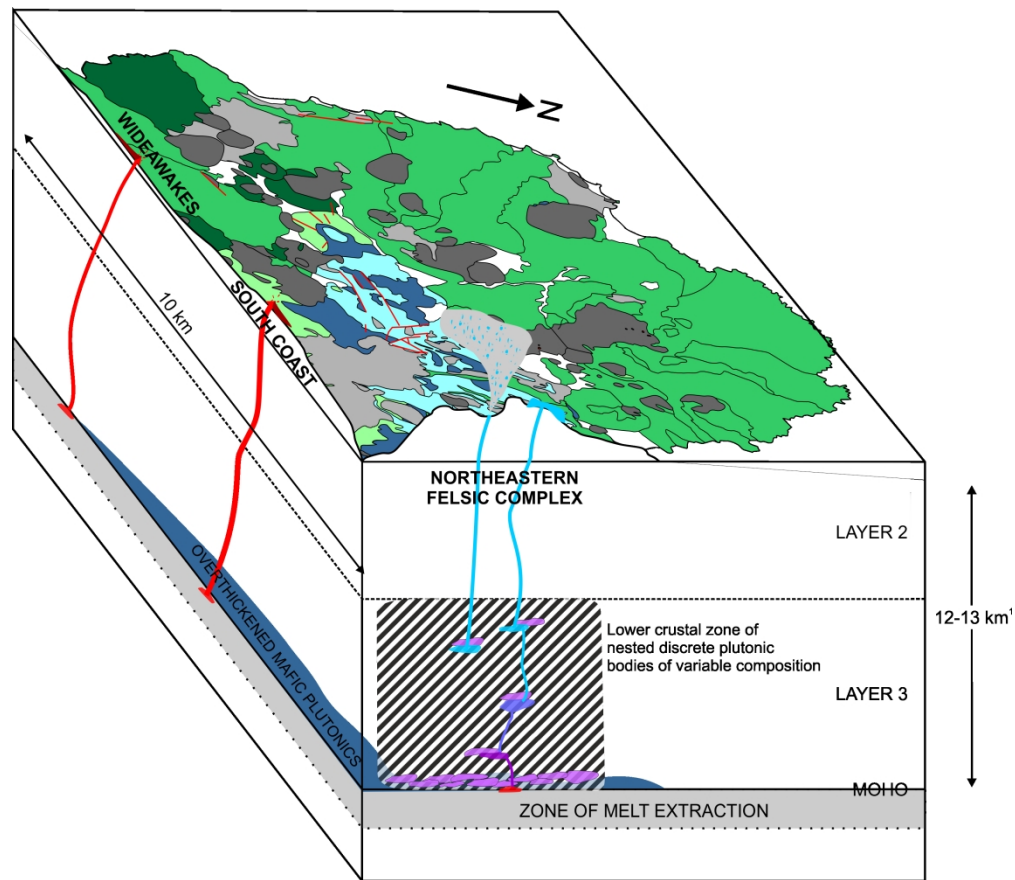


Figure 16: Magmatic plumbing system model for Ascension Island- magma storage regions are not to scale. Note the geographic variation in the distribution of plutonic bodies (mafic plutonics in blue, zone of nested felsic plutonics hashed, with examples in purple) within the crust. Ascent paths shown in red (mafic) and purple-blue (felsics). Crustal structure derived from Klingelhöfer et al. (2001).

Table 1: Samples investigated for this study

Sample number	Region	TAS classification	Sample type	Grid Reference (E, N)	Approximate age of sample
AI14-411	Youngest Sisters	Trachy-basalt	mafic lava	0568706, 9123576	zero age *
AI14-471	Older Sisters	Trachy-basalt	mafic lava	0567966, 9125332	> AI14-411‡
AI14-423	Youngest Letterbox	Trachy-andesite	mafic lava	0577052, 9121328	--
AI14-429	Older Letterbox	Trachy-andesite	mafic lava	0576443, 9121020	> AI14-423‡
AI14-445	Youngest Wideawakes	Basalt	mafic lava	0566907, 9117906	298 ka *
AI14-449	Older Wideawakes	Trachy-basalt	mafic lava	0568052, 9118271	> 298 ka ‡
AI14-522	Youngest South Coast	Basalt	mafic lava	0575056, 9119068	120 ka ""
AI14-514	Older South Coast	Basalt	mafic lava	0574092, 9119604	> 120 ka ‡
AI14-485	Ariane flow	Trachyte	felsic lava	0573518, 9124726	169 ka *
AI14-511	Cricket Valley	Trachyte	felsic dome	0574341, 0122098	52 ka *
AI14-428	White Horse	Trachyte	felsic dome	0575736, 9121232	zero age *
AI-94	Middleton's Ridge	Rhyolite	felsic lava	05693, 91214	1094 ka *
AI-103	Mountain Red Hill	Trachyte	felsic lava	05706, 91202	602 ka *
AI14-419	Letterbox felsic lava	Trachyte	felsic dome	0576780, 9120822	--
AI15-621	Devil's Riding School	Trachyte	felsic dome	0568897, 9120365	652 ka*
AI15-618	Youngest pumice fall	Trachyte	pumice fall	0573646, 9123128	--
AI14-435A	Echo Canyon	Trachyte	pumice flow	0573840, 9124754	--
AI14-438	NE scoria	Basalt	scoria fall	0573786, 9124790	--
AI14-493A	NASA unit E	Trachyte	pumice fall	0569420, 9120262	> AI14-488A ‡
AI14-488A	NASA unit A	Trachyte	pumice fall	0569475, 9120264	--
AI14-459A	Middleton's Valley fall	Trachy-andesite	pumice fall	0569849, 9120661	--
AI14-552	Green Mountain scoria	Basalt	scoria fall	0571584, 9121198	--
AI14-439A ⁺	Compositionally-zoned top	Trachy-andesite	zoned fall	0573786, 9124790	--
AI14-439D ⁺	Compositionally-zoned mid	Trachy-andesite	zoned fall	0573786, 9124790	
AI14-439G ⁺	Compositionally-zoned base	Trachyte	zoned fall	0573786, 9124790	

⁺ Data presented in Chamberlain et al., 2016.

* Ar-Ar age data from Jicha et al., 2014

"" K-Ar age data from Harris et al., 1992

‡ Stratigraphic relationship observed in the field

Table 2: Whole rock XRF data for Ascension samples, major elements in wt.%, trace elements in ppm.

Sample number	AI114-411	AI14-471	AI14-423	AI14-429	AI14-445	AI14-449	AI14-522	AI14-514	AI14-485	AI14-511	AI14-428	AI-94	AI-103
Location	Young Sisters	Old Sisters	Young Letterbox	Old Letterbox	Younger Wideawakes	Older Wideawakes	Younger South Coast	Older South Coast	Ariane	Cricket Valley	White Horse	Middleton's Ridge	Mountain Red Hill
SiO ₂	49.5	49.6	57.6	55.8	47.3	49.2	48.9	47.0	65.9	67.3	66.8	72.5	66.6
TiO ₂	3.12	2.97	1.42	1.58	3.44	3.26	2.25	2.79	0.42	0.37	0.41	0.23	0.45
Al ₂ O ₃	15.5	15.5	16.9	16.7	15.3	15.2	16.1	15.5	16.1	15.3	15.5	12.7	15.5
Fe ₂ O ₃	12.5	12.2	8.23	8.63	13.8	12.8	10.8	13.0	4.97	4.62	4.68	3.70	5.85
MnO	0.22	0.22	0.24	0.23	0.20	0.23	0.16	0.18	0.22	0.16	0.18	0.12	0.12
MgO	4.33	4.16	2.10	2.29	5.11	4.24	5.46	5.87	0.28	0.11	0.28	0.06	0.04
CaO	7.55	7.42	4.23	4.62	8.80	7.70	9.8	9.13	1.6	0.88	1.04	0.33	0.38
Na ₂ O	4.03	4.18	5.68	5.40	3.45	4.09	2.85	2.76	6.62	6.07	6.73	5.60	6.04
K ₂ O	1.41	1.50	2.53	2.37	1.08	1.44	0.80	0.77	3.71	5.11	4.30	4.72	4.94
P ₂ O ₅	0.89	1.03	0.60	1.04	0.81	1.18	0.53	0.4	0.09	0.06	0.09	0.03	0.06
LOI	-0.10	-0.02	-0.45	-0.51	-0.21	-0.34	0.24	-0.14	0.12	0.00	0.15	0.37	0.95
Total	99.0	98.8	99.0	98.1	99.1	98.9	97.8	97.3	100.1	100.0	100.2	100.4	101.0
Ba	254	263	553	503	183	266	194	120	780	554	919	69	644
Rb	32	34	53	50	24	29	17	16	76	117	94	126	81
Sr	455	461	381	410	423	458	501	391	135	7	24	1	4
Pb	18	20	20	21	17	19	bdl	bdl	5	8	6	10	5
Th	10	10	13	13	11	10	bdl	bdl	9	16	11	17	10
U	bdl	bdl	1	1	1	1	bdl	bdl	bdl	3.7	1.6	bdl	2.0
Zr	279	291	483	450	214	292	158	182	818	940	823	1266	756
Nb	52	55	80	77	42	54	28	29	135	151	139	177	121
Y	41	44	54	52	27	49	24	30	85	62	45	113	57
La	34	35	64	56	28	41	bdl	bdl	71	53	50	78	45
Ce	96	105	144	140	74	115	61	49	156	119	112	177	100
Sc	21	19	12	12	24	18	26	28	9	9	8	3	12
V	227	203	42	55	317	208	252	314	3	4	7	4	3
Ni	8	5	3	5	24	3	56	65	5	3	4	6	5
Zn	122	128	128	132	115	130	83	105	150	126	136	197	151
Sample number	AI114-419	AI15-621	AI15-618	AI14-435A	AI14-438	AI14-493A	AI14-488A	AI14-459A	AI14-552				
Location	Letterbox Felsic lava	Devils Riding School	Youngest Pumice fall	Echo Canyon	NE scoria	NASA unit E	NASA unit A	Middleton's Valley fall	Green Mountain scoria				
SiO ₂	65.5	66.9	65.0	65.6	48.2	68.1	64.3	58.5	47.7				
TiO ₂	0.32	0.33	0.33	0.31	2.49	0.18	0.33	1.06	2.85				
Al ₂ O ₃	15.9	15.4	13.7	15.7	16.1	13.1	14.5	17.6	16.0				
Fe ₂ O ₃	4.58	4.41	4.05	4.34	11.5	3.74	5.18	5.59	13.4				
MnO	0.17	0.17	0.16	0.20	0.19	0.11	0.19	0.16	0.18				

MgO	0.15	0.22	0.16	0.23	6.06	0.14	0.46	1.53	5.88
CaO	0.87	1.03	0.80	1.08	8.93	0.21	0.49	2.65	8.90
Na ₂ O	6.48	6.76	5.23	6.35	2.95	3.78	3.47	3.84	2.41
K ₂ O	4.06	4.68	4.84	4.00	1.15	5.66	4.88	2.72	0.60
P ₂ O ₅	0.57	0.04	0.07	0.04	0.94	0.02	0.03	0.37	0.31
LOI	0.27	0.93	4.57	2.70	-0.56	5.73	6.90	4.68	0.15
Total	98.9	100.9	98.9	100.5	97.9	100.8	100.7	98.7	98.3
Ba	898	1011	49	740	207	bdl	68	446	111
Rb	75	88	121	77	26	139	105	61	19
Sr	83	15	50	79	446	bdl	11	338	381
Pb	26	5	bdl	24	18	27	24	22	19
Th	17	10	20	16	10	27	20	14	10
U	2	3.4	bdl	bdl	1	bdl	bdl	1	1
Zr	818	1062	948	770	216	1301	1276	589	171
Nb	114	116	147	114	45	152	140	83	29
Y	76	73	89	72	35	96	88	52	28
La	95	57	109	91	34	135	127	64	17
Ce	157	117	173	162	94	188	186	124	47
Sc	6	10	bdl	bdl	23	bdl	bdl	6	28
V	2	4	bdl	bdl	209	bdl	bdl	34	307
Ni	3	7	bdl	bdl	65	bdl	bdl	6	45
Zn	138	145	141	142	111	171	179	103	105

Table 3: Petrography of Ascension lavas

Sample number	Region	TAS classification	Percentage Phenocrysts*	Vesicularity (%)	Fspar	Ol	Cpx	Cbt	Aeg	Glass	Ox+Accessory
AI14-411	Youngest Sisters	Trachy-basalt	<1 (f)	5	67	5	20				8
AI14-471	Older Sisters	Trachy-basalt	<1 (f)	7	68	10	17				5
AI14-445	Youngest Wideawakes	Basalt	3 (f, ol)	3	68	14	12				6
AI14-449	Older Wideawakes	Trachy-basalt	<1 (f, ol)	6	55	9	32				4
AI14-423	Youngest Letterbox	Trachy-andesite	<1 (f)	5	80	6	10				4
AI14-429	Older Letterbox	Trachy-andesite	2 (f)	43	77	8	9				6
AI14-522	Youngest South Coast	Basalt	40 (f, ol)	3	62	31	<1				7
AI14-514	Older South Coast	Basalt	18 (f, ol)	23	56	23					21
AI14-428	White Horse	Trachyte	2 (f)	24	64			29	4		3
AI14-511	Cricket Valley	Trachyte	6 (f, aeg)	1	78			12	9		1
AI14-485	Ariane flow	Trachyte	4 (f)	15	77			19			4
AI14-419	Letterbox felsic lava	Trachyte	<1 (f)	25	60		1	1		37	1
AI-103	Mountain Red Hill	Trachyte	2 (f, ox)	4	70			24	5		1
AI15-621	Devil's Riding School	Trachyte	3 (f)	13	68			27	4		1
AI-94	Middleton's Ridge	Rhyolite	<1 (f)	18	57			35	6		2

Arranged by relative age (see Table 1 and references therein)

Crystal percentages represent groundmass (<500 µm) crystals as well as those represented as phenocryst phases; Fspar = feldspar (plagioclase and ternary); Ol = olivine; Cpx = clinopyroxene; Cbt = cristobalite; Aeg = aegirine; Ox+Acc = bright in Back Scattered Electron imagery oxides and accessory phases including zircon and apatite.

*Phenocrysts used to represent phases > 500 µm in thin sectioned area. Phases which constitute phenocryst phases indicated in brackets: f= feldspar, ol = olivine; cpx = clinopyroxene; aeg = aegirine; ox = oxides;

Table 4: Representative feldspar data for Ascension samples

Sample	AI114-411				AI14-423		AI14-445		AI14-522		AI14-485		
Location	Young Sisters				Young Letterbox		Young Wideawakes		Young South Coast		Ariane		
Rock type	Trachy-basalt				Trachy-andesite		Basalt		Basalt		Trachyte		
Spot location	F3-C	F3-R	F5-C	F5-R	F1-C	F1-R	F5-C	F5-R	F1-C	F1-R	K3-C	K3-R	K10-C
SiO ₂	53.50	53.29	47.46	52.69	56.56	56.19	52.57	51.22	48.05	51.89	63.33	61.71	62.46
TiO ₂	0.16	0.17	0.05	0.13	0.04	0.06	0.13	0.16	0.05	0.10	0.00	0.01	0.01
Al ₂ O ₃	28.26	28.18	32.79	29.25	26.89	26.57	28.59	29.16	32.44	29.44	22.67	23.21	23.19
FeO*	0.91	0.92	0.45	0.77	0.37	0.49	0.77	0.87	0.46	0.66	0.20	0.24	0.25
MgO	0.10	0.09	0.13	0.11	0.04	0.05	0.12	0.13	0.15	0.15	0.00	0.01	0.01
CaO	11.45	11.61	16.66	12.19	8.93	8.88	12.20	12.80	15.92	13.46	3.48	4.44	4.28
Na ₂ O	5.04	5.10	2.30	4.74	6.55	6.63	4.48	4.29	2.67	4.17	9.17	8.56	8.87
K ₂ O	0.32	0.33	0.07	0.26	0.36	0.36	0.24	0.23	0.10	0.18	1.26	1.17	0.83
Total	99.76	99.70	99.91	100.15	99.75	99.23	99.10	98.87	99.86	100.05	100.11	99.34	99.90
An	54.6	54.7	79.7	57.8	42.1	41.7	59.3	61.4	76.3	63.4	16.1	20.8	20.0
Ab	43.5	43.5	19.9	40.7	55.9	56.3	39.3	37.2	23.1	35.6	76.9	72.7	75.3
Or	1.8	1.9	0.4	1.5	2.0	2.0	1.4	1.4	0.6	1.0	7.0	6.5	4.7
Sc	4.55	4.90	4.64	4.60	4.6	3.11	6.38	12.0	8.48	7.22	6.60	5.20	8.00
Ti	421	612	696	664	254	344	797	4970	508	526	136	137	147
V	0.53	1.60	1.73	1.58	0.42	0.51	3.49	83	3.12	2.41	0.16	bdl	0.48
Mn	32.8	32.6	36.5	38.8	37.7	36.9	37.9	323	37.8	28.3	27.0	25.0	27.0
Ga	21.2	20.0	24.9	23.0	24.8	26.0	24.7	22.9	23.1	23.1	28.2	27.1	26.8
Rb	0.31	0.45	0.28	0.14	0.86	0.56	0.93	2.90	0.24	0.32	1.56	1.64	1.29
Sr	1130	1096	1104	1168	1289	1317	922	811	793	718	834	883	836
Y	0.19	0.18	0.20	0.40	0.64	0.40	0.57	9.00	0.11	0.08	0.02	0.13	0.13
Zr	0.41	0.22	0.00	0.11	2.80	1.54	1.26	31.5	0.50	0.17	bdl	1.86	0.25
Ba	134	137	121	175	295	324	109	131	70.7	86.2	1248	1353	1087
La	3.16	2.76	2.46	2.71	5.88	6.40	2.13	9.23	1.08	1.10	8.29	7.78	7.35
Ce	5.21	3.73	3.61	4.33	8.62	6.47	4.00	20.0	1.93	1.55	9.14	9.42	8.43
Pr	0.54	0.41	0.24	0.42	0.90	0.81	0.37	2.33	0.17	0.18	0.74	0.57	0.60
Nd	2.24	0.99	1.00	1.55	2.10	2.36	1.72	11.4	0.59	0.70	1.71	1.80	1.51
Sm	0.23	0.09	0.34	0.41	0.57	0.19	0.31	2.37	0.04	bdl	0.13	0.00	0.17
Eu	1.07	0.68	0.78	0.98	3.04	2.50	0.68	1.21	0.38	0.39	8.97	9.59	9.15
Gd	0.17	0.27	0	0.25	0.35	0.20	0.25	2.44	bdl	0.06	bdl	0.21	0.17
Yb	bdl	bdl	bdl	bdl	0.13	bdl	0.01	0.61	0.02	bdl	0.00	0.00	0.00
Pb	0.40	0.22	0.26	0.22	0.84	0.65	0.23	0.63	0.22	0.10	1.04	1.01	0.84

Sample	AI114-485	AI14-511		AI14-419		AI14-435A		AI14-493A		AI14-488A		AI14-459A		
Location	Ariane	Cricket Valley		Letterbox felsic lava		Echo Canyon		NASA Unit E		NASA Unit A		Middletons Valley		
Rock type	Trachyte	Trachyte		Trachyte		Trachyte		Trachyte		Trachyte		Trachy-andesite		
Spot location	F10-R	F2-C	F2-R	F3-C	F3-R	F4-C	F4-R	F26-C	F26-R	K13-C	K13-R	K18-C	K18-R	K20-C
SiO ₂	65.60	65.20	65.89	65.20	64.76	65.21	65.91	67.98	68.53	68.51	67.88	62.04	61.39	58.09
TiO ₂	0.03	0.02	0.01	0.00	0.00	0.00	0.01	0.00	0.00	0.00	0.01	0.02	0.07	0.04
Al ₂ O ₃	19.42	19.33	19.00	20.71	20.90	21.22	20.57	19.24	19.53	19.36	19.31	22.50	23.09	24.64
FeO*	0.53	0.32	0.31	0.17	0.20	0.22	0.18	0.29	0.24	0.28	0.32	0.34	0.49	0.35
MgO	0.00	0.00	0.00	0.00	0.00	0.00	0.00	0.00	0.00	0.01	0.00	0.03	0.03	0.04
CaO	0.75	0.23	0.07	1.44	1.67	3.21	2.59	0.07	0.12	0.13	0.12	5.10	5.86	7.59
Na ₂ O	8.56	7.79	7.74	9.19	9.13	8.96	9.28	7.50	7.73	7.53	8.03	8.28	7.96	7.29
K ₂ O	4.37	6.30	6.54	2.40	2.46	1.12	1.40	6.64	6.36	6.08	5.92	0.94	0.74	0.48
Total	99.28	99.22	99.57	99.10	99.14	99.95	99.93	101.71	102.52	101.89	101.58	99.25	99.62	98.52
An	3.5	1.1	0.3	6.9	7.9	15.5	12.3	0.3	0.6	0.6	0.6	24.1	27.7	35.5
Ab	72.2	64.6	64.1	79.4	78.2	78.1	79.8	63.0	64.5	64.9	67.0	70.6	68.1	61.8
Or	24.3	34.4	35.6	13.7	13.9	6.4	7.9	36.7	34.9	34.5	32.4	5.3	4.2	2.7
Sc	6.90	6.77	7.44	0.33	6.97	3.90	5.20	6.30	3.20	5.20	6.90	5.20	4.20	3.60
Ti	156	104	76.5	6.89	124	105	104	62.0	84.0	69.8	67.7	229	264	352
V	0.31	0.45	0.17	0.02	bdl	0.11	bdl	bdl	1.70	0.09	0.01	bdl	1.40	1.70
Mn	20.1	1.20	0.60	2.55	7.00	22.1	11.8	1.10	bdl	2.10	bdl	19.9	28.0	34.8
Ga	27.8	25.6	24.5	0.95	28.7	28.0	25.9	32.2	34.7	30.7	35.3	29.5	23.5	33.9
Rb	2.40	39.0	47.3	0.33	10.2	2.06	1.91	51.2	45.7	32.8	33.0	1.56	2.16	1.18
Sr	828	1.31	0.81	13.0	222	644	571	0.79	2.28	2.35	1.46	1169	1230	1930
Y	0.31	0.17	0.03	0.19	0.79	0.04	0.00	0.00	0.00	0.00	0.00	0.10	0.27	0.36
Zr	2.70	3.22	0.45	2.17	bdl	0.00	0.00	bdl	2.90	0.30	0.47	bdl	5.50	1.80
Ba	1261	120	80.6	96.7	3770	1680	1552	66.0	129	194	97.4	533	753	448
La	8.60	0.67	0.42	0.48	6.96	7.35	6.03	0.65	0.66	0.43	0.56	11.6	12.4	11.7
Ce	9.90	0.68	0.23	0.73	8.47	8.37	7.14	0.13	0.30	0.37	0.17	15.2	14.2	15.9
Pr	0.74	0.02	bdl	0.07	0.72	0.48	0.52	0.00	0.00	0.00	0.00	1.01	1.14	0.85
Nd	2.40	0.27	0.04	0.28	2.20	1.47	1.24	0.00	0.00	0.00	0.00	3.10	3.60	3.10
Sm	0.26	0.03	bdl	0.05	0.22	0.00	0.00	0.00	0.00	0.00	0.00	0.00	0.00	0.27
Eu	9.82	0.98	0.99	0.28	7.07	8.85	8.50	0.73	1.00	1.25	1.00	2.27	3.65	3.53
Gd	0.18	0.01	bdl	0.04	0.35	0.00	0.00	0.00	0.00	0.00	0.00	0.00	0.04	0.00
Yb	0.00	bdl	bdl	0.02	0.00	0.00	0.00	0.00	0.00	0.00	0.00	0.00	0.00	0.00
Pb	1.21	1.12	0.93	0.07	1.94	1.29	1.34	0.53	0.88	0.89	0.69	1.91	1.85	1.02

Major element data given as wt.%; Anorthite, albite and orthoclase (An, Ab, Or) contents as mol. %; trace elements in ppm. For full data set, see Electronic Appendix 2. Where elements are below the detection limits of the method, bdl is written. Spot location refers to the analysis being core [C] or rim [R].

Table 5: Representative olivine major and trace element data for selected Ascension samples

Sample	AI14-411		AI14-423		AI14-445		AI14-522		AI14-435A		AI14-493A	
Location	Young Sisters		Young Letterbox		Young Wideawakes		Young South Coast		Echo Canyon		NASA unit E	
Rock type	Trachy-basalt		Trachy-andesite		Basalt		Basalt		Trachyte		Trachyte	
Spot tag	16_C	16_R	2_C	2_R	6_C	6_R	6_C	6_R	3_C	3_R	10_C	10_R
SiO ₂	39.59	38.43	35.49	35.07	38.96	37.31	37.93	37.17	29.42	29.23	28.74	29.11
Al ₂ O ₃	0.06	0.00	0.02	0.02	0.03	0.03	0.03	0.04	0.00	0.00	0.00	0.00
FeO*	14.67	24.67	32.21	32.30	19.05	28.37	22.89	29.63	59.56	59.01	62.61	61.38
MnO	0.22	0.76	1.10	1.13	0.25	0.48	0.33	0.56	4.96	4.94	5.53	5.48
MgO	43.65	34.97	30.98	30.87	41.46	34.30	38.63	32.92	3.77	3.73	0.83	0.98
CaO	0.22	0.26	0.18	0.18	0.25	0.26	0.34	0.32	0.31	0.32	0.31	0.52
Cr ₂ O ₃	0.03	bdl	0.00	0.00	0.01	0.00	0.00	0.00	0.00	0.00	0.00	0.00
NiO	0.19	0.00	0.01	0.00	0.15	0.04	0.07	0.05	0.02	0.00	0.00	0.00
P ₂ O ₅	--	--	0.10	0.04	0.01	0.04	0.01	0.03	--	--	--	--
Total	98.63	99.16	100.15	99.65	100.19	100.83	100.25	100.73	98.04	97.24	98.02	97.48
Fo (%)	84.1	71.7	63.2	63.0	79.5	68.3	75.1	66.5	10.1	10.1	2.3	2.8
Fa (%)	15.9	28.3	36.8	37.0	20.5	31.7	24.9	33.5	89.9	89.9	97.7	97.2

Major element data given as wt.%; Forsterite, fayalite contents as mol. %. For full data set, see Electronic Appendix 2. Spot location refers to the analysis being core [C] or rim [R].

Table 6: Representative clinopyroxene major element data for selected Ascension samples

Sample	AI14-423		AI14-429		AI14-449		AI14-522		AI14-485	AI14-511		AI14-428		AI14-419		AI15-621		AI15-618	
Location	Young Letterbox		Old Letterbox		Old Wideawakes		Young South Coast		Ariane	Weatherpost		White Horse		Letterbox bedrock		Devils Riding School		Young pumice fall	
Rock type	Trachy-andesite		Trachy-andesite		Trachy-basalt		Basalt		Trachyte	Trachyte		Trachyte		Trachyte		Trachyte		Trachyte	
Spot tag	2_C	2_R	GM	GM	1_C	1_R	1_C	1_R	GM	GM	GM	GM	GM	1_C	1_R	GM	GM	10_C	10_R
SiO ₂	48.35	50.51	49.37	36.12	50.22	48.46	50.63	47.34	47.79	47.74	47.90	50.81	50.86	48.50	48.20	47.94	49.82	51.82	51.58
TiO ₂	1.27	0.75	0.97	0.02	0.96	2.25	1.09	1.94	2.05	0.29	0.42	1.95	1.88	0.39	0.53	0.32	0.47	0.63	0.56
Al ₂ O ₃	3.62	1.98	3.03	0.02	2.15	5.37	2.82	5.19	2.59	0.29	0.33	2.35	3.50	0.70	0.89	0.21	1.99	1.59	1.69
FeO*	9.50	9.65	12.42	31.46	11.76	9.61	8.44	8.11	25.67	26.08	26.72	27.00	24.79	22.35	22.84	27.99	26.35	11.30	10.81
MnO	0.47	0.61	0.72	1.09	0.67	0.25	0.19	0.15	2.38	1.54	1.64	1.25	1.25	1.52	1.47	1.37	0.91	0.72	0.67
MgO	13.93	14.33	12.66	30.88	15.56	13.23	16.29	13.92	3.21	2.71	2.97	0.84	1.12	5.04	5.26	1.17	0.86	15.26	13.92
CaO	20.54	20.55	19.84	0.14	17.24	20.05	19.86	21.74	13.17	19.05	18.26	2.19	2.41	20.41	20.30	15.64	10.73	18.70	20.34
Na ₂ O	0.49	0.50	0.55	0.01	0.46	0.56	0.29	0.39	2.09	1.04	1.01	11.76	11.88	0.51	0.53	4.78	6.50	0.43	0.50
K ₂ O	0.00	0.03	0.00	0.00	0.01	0.00	0.00	0.01	0.09	0.00	0.00	0.70	1.24	0.01	0.01	1.39	2.06	0.00	0.01
Cr ₂ O ₃	0.00	0.00	0.00	0.00	0.00	0.00	0.13	0.23	0.00	0.00	0.00	bdl	bdl	0.00	bdl	bdl	0.00	0.00	0.00
Total	98.16	98.91	99.58	99.74	99.03	99.78	99.76	99.02	99.05	98.74	99.25	98.85	98.94	99.44	100.02	100.81	99.69	100.45	100.09

Major element data given as wt.%. For full data set, see Electronic Appendix 2. Spot location refers to the analysis being core [C], rim [R] or groundmass [GM].

Table 7: Representative glass analyses from Ascension Island
7a: Major element analyses normalised to 100 wt.%

Sample	AI14-419		AI15-618		AI14-552		AI14-438		AI14-435A			AI14-493A		AI14-488A		AI14-459A	
Location	Letterbox felsic lava		Young pumice		Green Mountain sc.		NE scoria		Echo Canyon			NASA unit E		NASA unit A		Middletton's Valley fall	
Spot Tag	419-1	419-2	15-5	15-6	1-1	1-4	14-1	14-2	10-2	10-3	10-4	8-1	8-4	15-1	15-2	4-1	4-3
SiO ₂	71.21	72.69	70.64	70.74	48.91	49.14	50.79	50.99	67.86	69.22	67.98	71.17	71.30	71.07	70.11	67.23	67.60
TiO ₂	0.27	0.31	0.19	0.19	3.68	3.72	3.61	3.52	0.10	0.29	0.22	0.21	0.22	0.17	0.18	0.48	0.49
Al ₂ O ₃	12.04	10.48	13.26	12.91	13.51	13.87	13.54	12.90	17.98	13.88	16.01	12.33	11.78	13.67	13.60	16.80	16.64
FeO*	5.64	5.77	4.50	4.89	13.53	13.27	12.02	11.97	1.38	4.47	3.43	4.77	4.87	3.28	3.96	2.78	2.94
MnO	0.27	0.28	0.27	0.25	0.15	0.23	0.19	0.20	0.08	0.19	0.16	0.18	0.16	0.12	0.20	0.07	0.06
MgO	0.06	0.07	0.03	0.02	5.32	5.41	3.78	4.52	0.02	0.08	0.09	0.02	0.02	0.00	0.00	0.54	0.50
CaO	0.77	0.51	0.48	0.46	9.70	9.43	7.91	8.56	0.65	0.64	0.90	0.29	0.28	0.46	0.45	1.32	1.23
Na ₂ O	5.15	4.44	6.14	6.11	3.34	3.16	3.48	3.22	7.32	5.43	6.09	5.52	4.42	4.42	4.95	5.88	5.73
K ₂ O	4.56	5.41	4.46	4.40	1.20	1.10	2.19	2.21	4.36	5.03	4.47	4.75	5.94	6.14	5.74	4.41	4.43
BaO	0.00	0.00	0.00	0.00	0.05	0.07	0.08	0.06	0.11	0.06	0.09	0.04	0.00	0.00	0.00	0.09	0.04
P ₂ O ₅	0.03	0.04	0.03	0.01	0.57	0.56	1.97	1.74	0.04	0.01	0.00	0.03	0.01	0.04	0.01	0.11	0.10
Cl	0.00	0.00	0.00	0.00	0.04	0.05	0.11	0.12	0.11	0.43	0.34	0.54	0.60	0.56	0.54	0.25	0.24
F	0.00	0.00	0.00	0.00	0.00	0.00	0.33	0.00	0.00	0.27	0.22	0.14	0.40	0.07	0.26	0.03	0.00
Total	100	100	100	100	100	100	100	100	100	100	100	100	100	100	100	100	100

Major element data given as wt.%. For full data set, see Electronic Appendix 2.

Table 7b: Selected trace element data from glass in felsic samples (all elements in ppm); where elements are below the detection limits of the method, bdl is written. Analyses in italics previously published in Chamberlain et al., 2016.

Sample	AI14-419		AI14-435A		AI14-493A		AI14-459A			AI14-439D		AI14-439G		
Location	Letterbox felsic lava		Echo Canyon		NASA unit E		Middleton's Valley fall			Compositionally-zoned mid (D) and upper (G)				
Tag	G1	G2	G1	G2	G1	G2	G1	G2	G3	G1	G2	G1	G2	G3
Li	10.0	15.0	10.0	17.0	15.5	29.0	24.0	bdl	13.0	13.6	18.0	29.0	20.0	18.0
Sc	13.6	15.9	13.8	12.8	9.70	9.40	5.00	11.1	13.0	11.2	21.0	27.0	10.1	27.0
Ti	994	1020	1705	1300	1448	1437	5400	4960	5400	2360	5690	4200	4530	2900
V	1.60	1.20	0.71	bdl	4.37	6.80	10.1	10.0	21.0	bdl	5.30	1.10	33.8	11.0
Mn	863	820	1544	1290	1259	1270	1720	1060	1190	1160	2720	2130	1290	1550
Zn	84	90	154	215	268	239	178	113	94	97	164	134	107	155
Ga	34	32	30	32	39	42	57	38	33	16	37	35	27	17
Rb	101	58	90	90	169	182	166	134	161	44	73	97	56	64
Sr	90	106	50	44	10	8	246	175	220	175	390	184	117	159
Y	76	49	77	80	124	129	52	44	38	34	74	70	41	79
Zr	930	584	791	868	1507	1661	1180	1000	1310	286	620	760	490	830
Nb	133	89	147	161	234	247	160	135	141	64	138	141	83	98
Ba	746	1240	790	720	55	61	950	651	1020	470	900	1290	840	1300
La	76	51	83	83	138	145	93	65	71	41	73	81	54	79
Ce	160	113	169	178	274	283	197	124	145	75	160	153	102	153
Pr	18	12	19	20	30	30	17	12	9	7	19	15	12	19

Nd	67	50	73	77	112	115	57	43	45	33	85	60	43	75
Sm	16.9	9.3	15.3	14.8	24.2	23.9	13.6	8.2	7.8	8	12.9	14.8	8.5	10.2
Eu	2.67	3.92	3.24	2.52	2.61	2.40	2.57	2.40	2.60	1.72	4.60	4.40	3.06	3.60
Gd	11.6	8.8	13.8	14.9	21.9	22.4	10.6	6.1	10.0	7.0	12.0	11.6	10.2	8.9
Dy	13.3	11.0	14.4	14.1	23.6	24.2	9.4	7.3	10.0	7.7	11.2	11.8	7.8	14.6
Er	8.10	5.66	8.45	7.91	12.93	13.39	5.30	5.20	4.70	3.70	8.10	7.40	4.40	4.90
Yb	8.70	6.70	7.97	7.48	11.91	13.00	4.60	5.20	6.20	3.60	7.80	6.70	2.50	5.50
Lu	1.18	1.00	1.15	1.15	1.61	1.76	1.18	0.81	0.60	0.27	0.99	0.59	0.37	0.51
Hf	18.6	12.7	17.1	19.2	30.3	33.8	26.8	21.0	23.5	6.9	12.8	14.5	9.2	13.2
Ta	7.2	5.0	8.5	9.0	13.3	13.4	11.1	9.5	6.9	3.2	6.8	6.1	4.5	6.9
W	2.50	0.79	1.88	1.95	3.58	4.00	5.50	2.77	1.90	0.54	2.00	1.03	1.00	1.14
Pb	5.91	4.65	6.75	6.79	14.37	13.06	13.50	10.20	4.30	2.90	4.10	6.30	3.50	6.20
Th	10.9	7.8	10.8	10.7	21.1	21.8	20.5	16.0	16.0	4.2	8.7	7.9	5.7	9.1
U	3.15	2.02	3.33	3.40	6.42	6.32	7.00	5.80	5.70	1.13	2.71	2.20	1.82	2.77

Table 8: Intensive variables modelled for Ascension Island samples

Sample number	Region	FeTi-Oxide Thermometry ¹		Feldspar-melt Thermometry ^{2,3}	
		T (°C)	fO ₂ (ΔNNO)	T (°C)	wt.% H ₂ O ⁴
AI14-411	Youngest Sisters	935	-0.4	1150	
AI14-471	Older Sisters	--	--	1152	
AI14-423	Youngest Letterbox	990	-0.05	1093	
AI14-429	Older Letterbox	1025	+0.08	1110	
AI14-445	Youngest Wideawakes	985	-0.34	1167	
AI14-511	Cricket Valley	884	-1.6	886	5.2
AI14-428	White Horse	--	--	837	5.5
AI-94	Middleton's Ridge	--	--	772	4.7
AI-103	Mountain Red Hill	967	-1.9	801	7.2
AI14-419	Letterbox felsic lava	--	--	837	
AI15-621	Devil's Riding School	--	--	871	5.1
AI15-618	Youngest pumice fall	--	--	847	6.4
AI14-435A	Echo Canyon	--	--	993	
AI14-438	NE scoria	--	--	1164	
AI14-493A	NASA unit E	--	--	811	7.1
AI14-488A	NASA unit A	--	--	813	8.1
AI14-459A	Middleton's Valley fall	950	-0.2	1034	
AI14-552	Green Mountain scoria	--	--	1174	
AI14-439A*	Compositionally-zoned scoria	845	-2.28		
AI14-439G*	Compositionally-zoned pumice	866	-1.94		

¹Using the calibration of Ghiorso & Evans, 2008, on oxides which have passed the equilibrium test of Bacon & Hirschmann (1988).

² Plagioclase-melt thermometry from Putirka (2008), only analyses where $K_D(\text{Ab-An})$ was 0.1 ± 0.11 for $T < 1050$ °C, or 0.27 ± 0.05 at $T > 1050$ °C were used (Putirka, 2008).

³Alkali-feldspar-melt thermometry (Putirka, 2008). Only analyses within the equilibrium bounds outlined in Mollo et al. (2015) were used.

⁴ Alkali-feldspar-melt hygrometry (Mollo et al., 2015). Only analyses within the equilibrium bounds outlined in Mollo et al. (2015) were used. Uncertainties of ± 0.7 wt.% consistent with that published in Mollo et al. (2015) are assumed.